
DEEPRED: AN ARCHITECTURE FOR REDSHIFT ESTIMATION

Alessandro Meroni^{1,*}, Nicolò Oreste Pincioli Vago^{1,2,*}, and Piero Fraternali¹

¹Department of Electronics, Information and Bioengineering, Politecnico di Milano, Milan, Italy

²INAF – Osservatorio Astronomico di Roma, Monteporzio Catone, RM, Italy

^{*}Equal contribution

{alessandro5.meroni, nicoloreste.pincioli, piero.fraternali}@polimi.it

ABSTRACT

Estimating redshift is a central task in astrophysics, but its measurement is costly and time-consuming. In addition, current image-based methods are often validated on homogeneous datasets. The development and comparison of networks able to generalize across different morphologies, ranging from galaxies to gravitationally-lensed transients, and observational conditions, remain an open challenge. This work proposes DeepRed, a deep learning pipeline that demonstrates how modern computer vision architectures, including ResNet, EfficientNet, Swin Transformer, and MLP-Mixer, can estimate redshifts from images of galaxies, gravitational lenses, and gravitationally-lensed supernovae. We compare these architectures and their ensemble to both neural networks (A1, A3, NetZ, and PhotoZ) and a feature-based method (HOG+SVR) on simulated (DeepGraviLens) and real (KiDS, SDSS) datasets. Our approach achieves state-of-the-art results on all datasets. On DeepGraviLens, DeepRed achieves a significant improvement in the Normalized Mean Absolute Deviation (NMAD) compared to the best baseline (PhotoZ): 55% on DES-deep (using EfficientNet), 51% on DES-wide (Ensemble), 52% on DESI-DOT (Ensemble), and 46% on LSST-wide (Ensemble). On real observations from the KiDS survey, the pipeline outperforms the best baseline (NetZ), improving NMAD by 16% on a general test set without high-probability lenses (Ensemble) and 27% on high-probability lenses (Ensemble). For non-lensed galaxies in the SDSS dataset, the MLP-Mixer architecture achieves a 5% improvement over the best baselines (A3 and NetZ). In addition, SHapley Additive exPlanations (SHAP) shows that the models correctly focus on the objects of interest with over 95% localization accuracy on high-quality images, validating the reliability of the predictions. These findings suggest that deep learning architectures are a scalable, robust, and interpretable solution for redshift estimation in future large-scale surveys comprising heterogeneous astronomical objects.

Keywords Redshift estimation · Gravitational lenses · Explainable Artificial Intelligence · Ensemble learning

1 Introduction

Astrophysics is the branch of astronomy that employs the principles of physics and chemistry to ascertain the nature of astronomical objects [1]. Astrophysics has led to the discovery of new phenomena, such as gravitational lenses [2], spatio-temporal distortions caused by the gravitational field of massive objects. When an astronomical source is behind a gravitational lens relative to an observer, it appears distorted, often forming structures like Einstein rings [3] and Einstein crosses [4].

Time-domain astronomy [5] studies transient astronomical events (i.e., short-lived events with durations ranging from fractions of a second to years), such as supernovae [6] and pulsars [7, 8, 9, 10, 11]. Supernovae are powerful and luminous stellar explosions that occur during the last evolutionary stages of a massive star. Gravitational lenses can distort supernovae, giving origin to gravitationally-lensed supernovae [12, 13, 14], a rare phenomenon that allows cosmological studies and the testing of relativity.

Redshift is the shift of an object's spectral lines toward longer wavelengths (i.e., toward red in the visible spectrum) compared to a reference. This phenomenon can occur due to the universe's expansion (cosmological redshift [15]),

the relative motion of the object with respect to the observer (Doppler redshift [16, 17]), or strong gravitational fields (gravitational redshift [18]). Redshift can be estimated either through spectroscopy (spectroscopic redshift, based on the analysis of objects' spectra) or photometry (photometric redshift, based on measurements of objects' brightness across different frequency ranges). Redshift has several applications in astrophysics, including estimating distances between astronomical objects [19], creating 3D maps of the universe [20], and estimating the universe expansion rate [21].

Modern astrophysics benefits from large amounts of data [22, 23] acquired by ground-based and space telescopes across multiple wavelengths (e.g., in the optical and X-ray bands). Large-scale surveys, such as Large Synoptic Survey Telescope (LSST) [24], are expected to generate petabytes of data [25]. Handling large amounts of data presents significant challenges, including data storage, processing, and analysis, making manual analysis impractical. For this reason, data-driven techniques are necessary.

Artificial Intelligence (AI) can support data-driven tasks in astrophysics, as it allows the analysis of large amounts of data, including the classification of objects [26] and their automated detection. The work in [27] uses Machine Learning (ML) to classify stars, the work in [28] uses computer vision to study solar activity, and the work in [29] uses deep learning to detect and classify exoplanet candidates with high precision automatically. The works in [30, 31] focus on redshift estimation and highlight the challenges in obtaining spectroscopic redshifts, which require significant telescope time and human resources. The work in [32] estimates redshifts for quasars using ML, and the work in [33] proposes Convolutional Neural Networks (CNNs) and Deep Learning (DL) for redshift estimation. Ensuring the trustworthiness of AI models remains a significant challenge in astrophysics, as not all the existing DL algorithms used in this field are interpretable. The survey in [34] presents an overview of interpretability methods for AI in astronomy.

The primary goal of this work is to estimate redshift for gravitational lens sources and galaxies using Computer Vision (CV) algorithms. For this purpose, we use two real datasets and four simulated labelled datasets.

The four simulated datasets contain $\approx 15,000$ gravitational lenses each and are extracted from the DeepGraviLens (DGL) dataset [35, 26, 36]. These datasets replicate the observations captured with LSSTCam [37] or DECam [38]. The Kilo-Degree Survey (KiDS) real dataset comprises $\approx 4,500$ candidate gravitational lenses, classified in [39] and retrieved from the European Southern Observatory (ESO) Science Archive Facility. Each image is paired with a photometric redshift estimated using more spectral channels than those available in the image itself. This dataset serves as an additional validation of the model's performance in a real scenario. The Sloan Digital Sky Survey (SDSS) real dataset comprises $\approx 517,000$ galaxies, paired with spectroscopic redshifts. We intentionally consider heterogeneous regimes to test the limits of image-only redshift estimators. We apply the same pipeline to different morphologies and data (simulated vs. real) to demonstrate that modern computer vision backbones can estimate redshift independently of specific object types or Point Spread Functions (PSFs).

The contributions of this work can be summarized as follows:

- We introduce the architecture of DeepRed, a pipeline that takes as input images of astronomical observations and produces as output redshift estimates. DeepRed uses complementary sub-networks trained independently and ensembles their outputs by means of a Linear Regression Ensemble (LRE).
- We evaluate the designed architecture on the four simulated DGL datasets [35], on the real KiDS dataset and on the real SDSS dataset.
- We compare DeepRed with Histogram of Oriented Gradients (HOG) + Support Vector Regressor (SVR), A1 [40], A3 [40], NetZ [31] and PhotoZ [41] using a set of established metrics in redshift estimation (Normalized Mean Absolute Deviation (NMAD), σ_{68} , bias and outlier rate). DeepRed yields NMAD improvements ranging from $\approx 46\%$ to $\approx 55\%$ on the simulated datasets and from $\approx 5\%$ to $\approx 29\%$ on the real datasets.
- We use SHapley Additive exPlanations (SHAP), an explainability algorithm, to show that DeepRed focuses on the relevant parts of the images (i.e., the astronomical objects) rather than on irrelevant areas of the background. To quantify the explainability results, we extract the most influential pixel for each image and compute the localization accuracy with respect to the astronomical object bounding box (over 95% on datasets with less noise).
- We demonstrate that DeepRed generalizes well across datasets with different observational conditions, showing its suitability for future large-scale sky surveys.

To summarize, DeepRed is a methodological framework and ensemble pipeline, rather than a single new neural network architecture. While the individual components rely on established backbones, the primary contribution is the integration of distinct architectural families, to exploit their differences. Furthermore, DeepRed incorporates explainable AI not only as a post-hoc analysis, but as a validation tool that ensures that the redshift predictions are derived from the most relevant parts of the images.

The rest of the paper is organized as follows: Section 2 presents an overview of the state of the art and the astrophysics background concepts; Section 3 presents the dataset, the metrics, and the algorithms used in this work; Section 4 presents quantitative results and explainability results; Section 5 presents the conclusions and discusses potential future directions for research based on this work.

2 Related work

ML is a branch of AI that focuses on systems that can learn from data. DL is a branch of ML that uses Artificial Neural Networks (ANNs) formed by multiple layers and allows to learn complex patterns in data. It can handle different types of data [42], including tabular data, images, and sequential data (e.g., time series and videos).

The work in [42] identifies three main architecture categories: Multi-Layer Perceptron (MLP) (for tabular data), CNN (for images), and Recurrent Neural Network (RNN) (for sequential data). Since 2017, transformers [43] have been used to address Natural Language Processing (NLP) tasks and are now also used for vision tasks. Vision Transformers (ViT) [44] model images as sequences of patches, each enriched with positional information. They apply self-attention to all patch pairs, focusing on the most relevant regions and capturing global dependencies across the image. Compared to CNNs, transformers are better at modeling long-range relationships. Variants like Swin Transformer (SwinT) [45] incorporate hierarchical designs and local attention to balance detailed and generic understanding of the images.

CV is an interdisciplinary field concerned with the automatic extraction of information and patterns from images [46]. It has advanced over the years, driven by improvements in DL architectures. Traditional methods such as Scale-Invariant Feature Transform (SIFT) [47], HOG [48], and edge detection algorithms like Canny [49] extract features that can be combined with classifiers like Support Vector Machine (SVM) or regressors like SVR [50]. These methods are effective for datasets with fewer data but are less effective than CNNs on bigger datasets [42]. DL revolutionized computer vision, becoming common for solving modern vision tasks. ResNet-based [51] and transformer-based architectures, for instance, are effective at object detection and segmentation.

Image regression is a type of regression task in CV, where the input is an image and the output consists of one or more continuous numerical variables, rather than class labels. Image regression has several applications, such as medicine [52] and environmental monitoring [53]. The work in [54] addresses the task of counting objects in ecological surveys, and the work in [36] extends image regression to the case of multimodal astronomical data.

Ensembling is an approach to improve prediction performances starting from the predictions of multiple ML models. The survey in [55] presents diverse ensembling applications, ranging from medical diagnosis to fraud detection and astrophysics. The work in [56] uses ensembling for pulsar candidate classification, and the work in [26] uses ensembling for gravitationally-lensed supernovae classification. Ensembling methods, used for both classification and regression, include key techniques like stacking, boosting, and bagging [55].

DL architectures are often considered black-box models due to their complexity, making their decision processes hard to interpret. Explainable Artificial Intelligence (XAI) addresses this challenge by enabling the interpretation of DL outputs, with several key goals: to justify the model’s outputs (*explain to justify*), assess and monitor decisions to detect vulnerabilities or biases (*explain to control*), identify areas for performance improvement (*explain to improve*), and uncover new patterns and insights (*explain to discover*) [57]. The work in [57] presents several XAI techniques. Grad-CAM [58] is a variant of Class Activation Map (CAM) that creates heatmaps highlighting important regions of the input image, using gradients from the target class to compute the importance of each region. Still, the most effective CAM variant depends on the specific problem [58, 59, 60, 61]. Local Interpretable Model-Agnostic Explanations (LIME) [62] uses simple surrogate models to approximate the predictions of the underlying model. Layer-wise Relevance Propagation (LRP) [63] creates a heatmap of the input by working backwards from the output, starting from the last layer. Finally, SHAP [64] is a game-theoretic approach for explaining machine learning model outputs by perturbing input data and measuring how much the predictions change. Compared with LRP and CAM-based algorithms, SHAP is model-agnostic, making it a more versatile approach. Compared with LIME, SHAP is regarded as easier to interpret in [65].

Time-domain astronomy studies transient astronomical events, such as supernovae (i.e., powerful and luminous explosions of stars occurring during the last evolutionary stages of massive stars), pulsars (i.e., highly magnetized rotating neutron stars that emit beams of electromagnetic radiation out of their magnetic poles) [66], and gravitationally-lensed transients (i.e., the spatio-temporal distortion caused by massive objects such as galaxies and black holes lensing transient phenomena).

One key aspect of understanding these phenomena is determining their redshift, which provides information about their distance and the expansion of the universe. Redshift can be estimated using spectroscopic and photometric methods [67]. The spectroscopic redshift [68] uses emission spectra (i.e., the light emitted over a range of energies), which are

determined by the chemical composition of astronomical bodies. In the case of redshift, the spectra are shifted with respect to theoretical predictions, making it measurable. This method is time-consuming and requires high-quality and expensive spectroscopes for accurate measurements. Photometric redshift [69] compares data of new and already known astronomical objects using brightness values for specific energy bands. This method is faster and cheaper than spectroscopic redshift, but also less accurate.

ML has demonstrated its effectiveness in estimating both photometric and spectroscopic redshifts from images. The work in [70] applies ML to photometric measurements, specifically the magnitudes of five filters (in the *ugriz* photometric system). An artificial neural network, ANNz2, is then trained to estimate the photometric redshift. The work in [32] uses three tree-based machine learning algorithms trained on photometric measurements to extract the photometric redshift of quasars. The work in [71] uses a simulated dataset and trains a neural network, SYTH-Z, on photometric data to predict photometric redshift. It uses input from five bands (*ugriz*), which are combined before being processed by the neural network. The work in [33] uses Fully Connected Networks (FCNs) for redshift estimation, comparing them with tree-based machine learning models. Still, these works use tabular data rather than entire images. CNNs are starting to be used to predict redshift directly from images to capture additional spatial and morphological information for improved redshift estimation. In [30], the authors use CNNs to estimate the redshift on 64×64 pixel images of galaxies. They use a CNN taking in input images with 5 channels (*ugriz*), but they do not use explainability to interpret the model’s predictions. The architecture is formed by two convolutional layers alternated with pooling layers. Then, the output of the final layer is flattened and processed by a series of dense layers to estimate the redshift value. In [31], the authors use NetZ, which takes as input images with 5 channels (*grizy*), but still do not use explainability techniques. The architecture is formed by two convolutional layers with max pooling and three Fully Connected (FC) layers. In [72] the authors propose PhotoZ, which exploits morphological labels during training, different from other image-only pipelines. The work in [73] estimates the distribution of the photometric redshift from a high-dimensional image. The architecture takes images with 15 bands as input, and no explainability methods are used. The architecture consists of three convolutional layers alternated with pooling layers. The output of the last convolutional layer is used as the input for two Mixture Density Network (MDN) layers in order to retrieve the probabilistic distribution of the redshift. Finally, [40] presents two CNN architectures, A1 and A3, which take as input only images to estimate redshift, and proposes SHAP to explain the predictions. Still, none of these works considers the case of gravitationally-lensed transients, such as gravitationally-lensed supernovae, most do not use explainability techniques to clarify the predictions or decision-making processes of their models, and none provides a quantitative evaluation of the explainability algorithms’ outputs. The work in [26] provides four simulated datasets, containing gravitationally-lensed supernovae, and can be used as a benchmark for redshift estimation.

2.1 Positioning with respect to the state of the art

While recent literature has investigated the use of deep learning for redshift estimation, this work introduces advancements that distinguish DeepRed from existing methodologies. First, state-of-the-art works in redshift estimation rely on custom neural networks, such as NetZ and PhotoZ, or traditional ML regressors. In contrast, DeepRed is the first framework to systematically adapt generic CV architectures (specifically EfficientNet, SwinT, and MLP-mixer (MLPm)). By using these backbones, which are standard in computer vision but underutilized in this domain, we demonstrate that generic architectures can significantly outperform domain-specific models, such as A1 and A3, without requiring specialized, handcrafted designs. Second, this is the first study to systematically evaluate redshift estimation for gravitationally lensed transients, such as lensed supernovae. Existing studies primarily focus on galaxies or quasars, while our work validates performance across heterogeneous morphologies (e.g., Einstein rings and lensed supernovae) to prepare for surveys like LSST, where rare transient phenomena will be the targets of cosmological studies. Finally, while XAI tools like SHAP have been evaluated qualitatively in previous studies, DeepRed proposes a quantitative evaluation of explainability results. We define formal metrics (localization accuracy and the normalized distance between the most influential pixel and the astronomical objects’ centers) to validate that the model is focusing on relevant areas of the images.

3 Datasets and methods

3.1 Datasets

All the datasets consist of astronomical images that contain gravitational lenses, gravitationally-lensed supernovae, and/or galaxies. Every image is paired with a redshift. In the simulated DGL datasets, the Ground Truth (GT) redshift is the one used to generate the data [26, 74, 36], while in the real datasets the redshift is measured. The rarity of gravitational lenses, particularly for gravitationally-lensed transients, combined with the limited availability of spectroscopic redshift data, prevents the use of large real datasets for redshift estimation on gravitational lensing data.

As a result, simulated datasets are commonly employed, especially in studies involving gravitationally-lensed transients. All the datasets are divided into a training set, used to update the models' parameters, a validation set, used for early stopping and hyperparameters selection, and a test set.

3.1.1 DeepGraviLens

The four simulated DGL datasets are introduced in [26], with the simulation details described more extensively in [74], and the datasets made publicly available at [35].

The datasets consist of images categorized into four classes:

- No Lens: images containing only non-lensed objects, such as stars and galaxies.
- Lens: images of galaxy-galaxy lenses, where both the source and the lens are galaxies.
- Lensed Supernova of type Ia (LSN_{Ia}): lenses with Type Ia supernovae as the background source. These supernovae result from the thermonuclear explosion of a white dwarf (see also [75]).
- Lensed Supernova of type core-collapse (LSN_{cc}): lenses with core-collapse supernovae as the background source, typically originating from the collapse of massive stars (see also [75]).

This work uses images from the classes Lens, LSN_{Ia}, and LSN_{cc} to estimate the redshift. The class "No Lens" has been excluded, as it does not include gravitational lenses.

DGL comprises four simulated datasets (see also Figure 1):

- LSST-wide: images from LSST, acquired with the LSSTCam camera [37]. Each pixel corresponds to 0.2 arcseconds. The exposure time is 30 seconds. The simulation reflects observational conditions estimated for the first year of the LSST survey [76].
- DESI-DOT: images from the DECam instrument [38], based on real observing conditions from the Dark Energy Survey (DES) wide-field survey [77]. The exposure time is 60 seconds.
- DES-deep: images from DECam [38], following the observing conditions of the DES SN program [78] and has an exposure time of 200 seconds.
- DES-wide: images from DECam [38], under the real observing conditions of the DES wide-field survey [77]. The exposure time is 90 seconds.

DESI-DOT, DES-deep and DES-wide have the same scale of 0.263 arcseconds per pixel. All datasets contain 45×45 pixels images with 4 channels in the *griz* photometric system and are divided into 70% for training (≈ 10000 samples), 15% for validation (≈ 2200 samples) and the last 15% for testing (≈ 2200 samples). Figure 1 shows an example image from each dataset, each featuring an Einstein ring. Since the DGL datasets are entirely simulated, each sample is unique, thus preventing data leakage across subsets.

3.1.2 KiDS

The KiDS dataset contains images retrieved from the Kilo-Degree Survey [79], using the ESO Science Archive Facility [80]. It comprises both low-probability and high-probability lenses. We use 4-channel images in the *ugri* photometric system because of the limited availability of images with the *z* channel in the archive. To ensure consistency between samples with and without gravitational lenses, the observations have AB magnitudes (i.e., standardized logarithmic measurements of brightness) between 20 and 25.5. The images were cropped to 45×45 pixels and have 0.2 arcsec/pixel, similar to the DGL datasets.

The dataset consists of $\approx 4,500$ candidate low-probability lenses and a subset of 264 high-probability lenses, similar to [39]. The low-probability lenses are split into training ($\approx 70\%$), validation ($\approx 15\%$), and test ($\approx 15\%$) sets. The high-probability lenses are used as an additional test set (the "lens set"). Figure 2 shows an example image in the lens set. Each image is associated with a photometric redshift, estimated as presented in [81], because of the scarcity of spectroscopic redshift measurements in the lens set. Each image is centered on a different position, thus no duplicates can be found in the dataset. Nearby objects may occasionally appear in images assigned to both the test set and the training or validation sets. However, these instances refer to distinct central objects, each associated with a different redshift. To assess potential data leakage, we considered the set of 137 couples of nearby objects, defined as those separated by angular distances compatible with an image dimension (≈ 13 arcsec). Then, for each couple we analyzed the correlation between the distances and the absolute differences in their redshifts. The resulting Pearson correlation coefficient is negligible (≈ 0.06), confirming that the presence of nearby sources does not introduce data leakage.

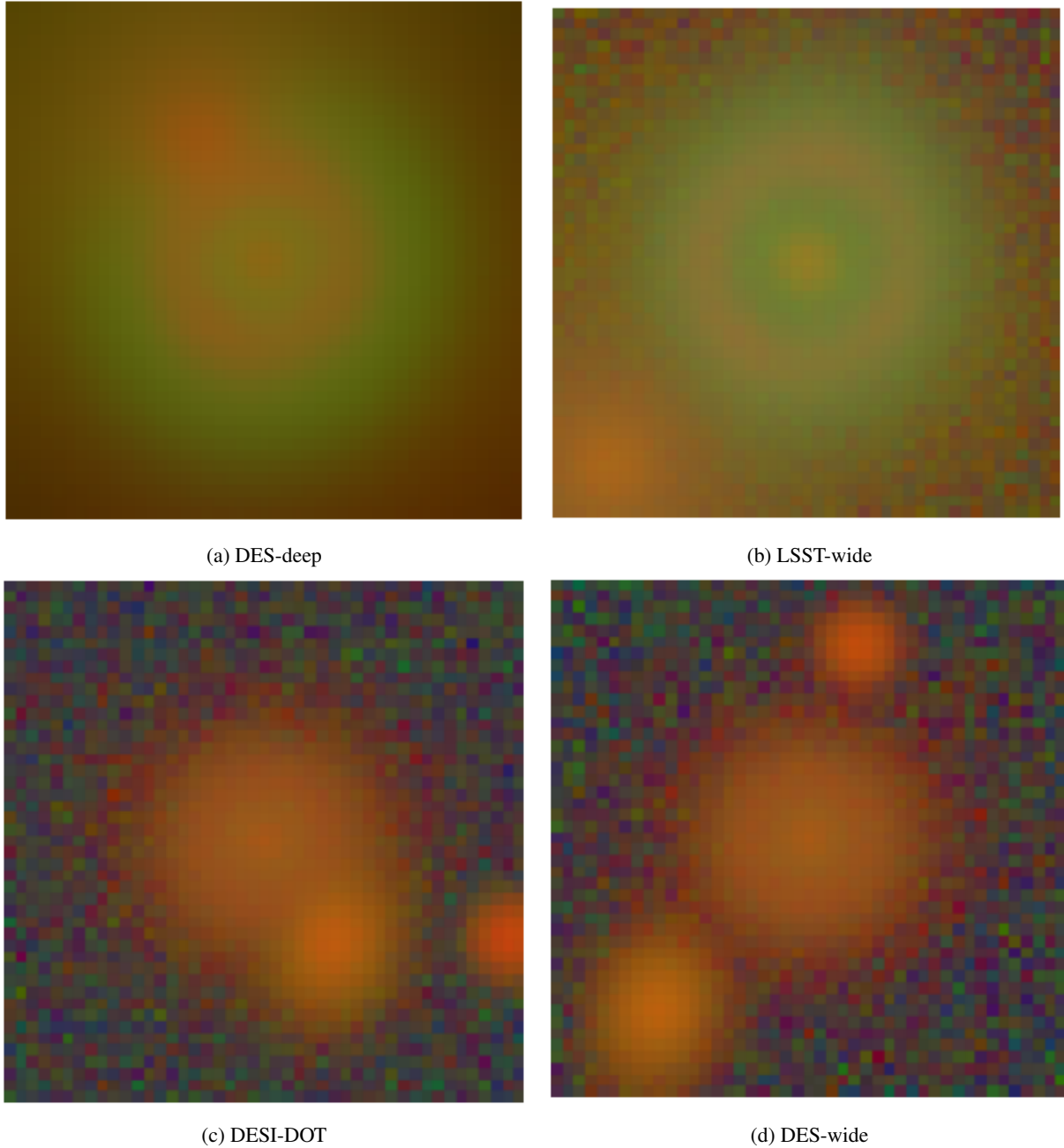


Figure 1: Examples of Einstein ring images in the four DGL datasets. DESI-Deep, DESI-DOT and DESI-wide have a side of ≈ 12 arcsec, and LSST-wide has a side of ≈ 9 arcsec.

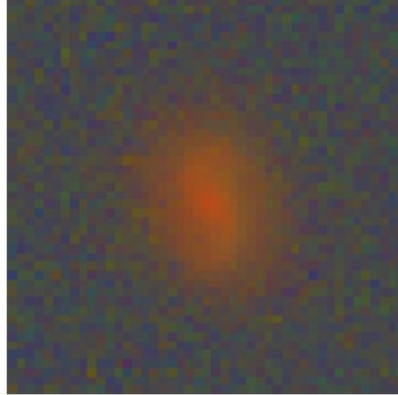


Figure 2: Example of high-probability lens in the KiDS dataset. Each side corresponds to ≈ 9 arcsec.

Filters	Spectral range
u	327-383 nm
g	406-539 nm
r	561-697 nm
i	682-838 nm

Table 1: Bands of the channels used for the SDSS dataset.

3.1.3 SDSS

The SDSS dataset comprises the data introduced in [41], consisting of galaxies observed in five channels corresponding to the *ugriz* filter system. This dataset is used to benchmark and compare the performance of proposed architectures against the current state-of-the-art methods for redshift estimation on non-lensed galaxies. Every image is paired with the spectroscopic redshift as GT. The dataset is divided into $\approx 80\%$ train set, $\approx 10\%$ validation set, and $\approx 10\%$ test set, consistently with the implementation presented in [40], available on <https://github.com/1ArgoS1/PhotoZ> (as of July 2025). The images were cropped to $45 \times 45 \times 5$ pixels for consistency with the other datasets presented in this work. Each image is centered on a source of interest as presented in [41]. The lack of data leakage is guaranteed by the uniqueness of the analyzed sources.

3.2 Tasks, targets and outputs

The main task of this work is redshift estimation from astronomical observations and is formulated as a regression problem from multi-band 45×45 pixels images. Training targets are derived from either simulations or redshift measurements. The second task is explainability, which shows where the best models focus their attention. For each image and predicted redshift, we use SHAP heatmaps to highlight the most influential pixels. We perform a quantitative evaluation of the SHAP heatmaps by comparing the most influential regions against the position of the gravitational lenses. First, we define the ground truth bounding boxes. These are generated automatically by computing the maximum intensity across image channels and selecting the pixels with the top 10% intensity values. The resulting bounding boxes are then manually validated. Then, we analyze the SHAP heatmaps. We identify the most influential pixel in each image as the global maximum of each SHAP heatmap. We then compute two metrics: the distance between this peak value and the lens center, and the localization accuracy (i.e., the percentage of times the peak SHAP points fall within the bounding boxes). Overall, high localization accuracy and low mean and median values indicate that the models focus on the most relevant parts of the images, while low localization accuracy and high mean and median values either indicate that the model does not focus on the correct parts of the images or that the object of interest spreads across the entire image (as in the case of DES-deep).

Figure 4 compares the GT redshift distributions for DGL (a - the four datasets have the same distribution), KiDS (b and c), and SDSS (d). The four distributions have different mean values (ranging from 0.11 to 0.49), median values (ranging from 0.10 to 0.51), and skewnesses (negative for DGL, positive for KiDS test set and SDSS and no skewness for KiDS lens set). These differences allow the evaluation of the models' robustness across diverse scenarios.

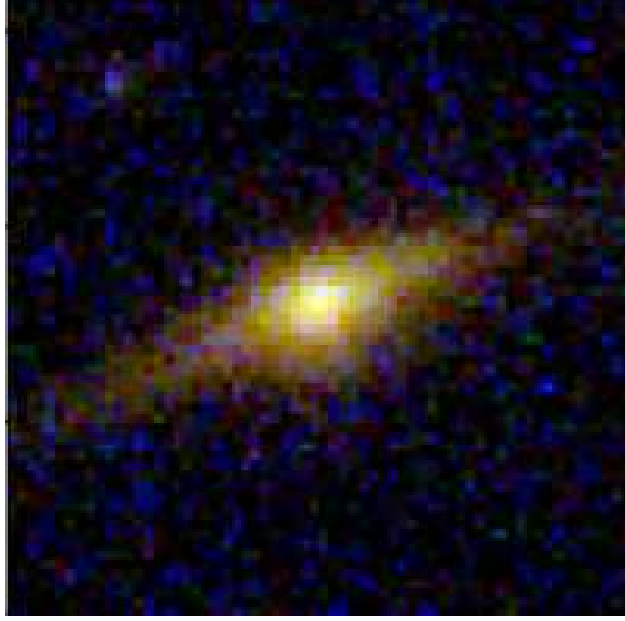


Figure 3: Example of an image taken from SDSS. Each side corresponds to ≈ 18 arcsec.

3.3 Loss functions and metrics

The Mean Square Error (MSE) is defined as:

$$MSE = \frac{1}{N} \sum (y_i - \hat{y}_i)^2 \quad (1)$$

where N is the number of samples, y_i is the label of the sample i (i.e., the GT redshift) and \hat{y}_i is the value predicted by the model for sample i . MSE penalizes larger errors heavily due to the squaring of residuals, discouraging large deviations from GT values.

Mean Absolute Error (MAE) is defined as:

$$MAE = \frac{1}{N} \sum |y_i - \hat{y}_i| \quad (2)$$

Different from MSE, MAE uses the same units as the redshift.

R^2 is defined as:

$$R^2 = 1 - \frac{\sum (y_i - \hat{y}_i)^2}{\sum (y_i - \bar{y}_i)^2} \quad (3)$$

where \bar{y}_i is the average value of the redshift in the dataset. R^2 is a standard metrics for regression problems (see e.g. [54, 82]). The closer the R^2 is to 1, the better the estimator is because it indicates a low estimation error compared to the variance.

The NMAD is a robust estimator of the variance, defined as:

$$NMAD = 1.4826 \cdot \text{median} \left(\left| \frac{\hat{y}_i - y_i}{1 + y_i} \right| \right) \quad (4)$$

Unlike standard deviation, NMAD is less sensitive to catastrophic outliers, making it a preferred metric for photometric redshift performance.

σ_{68} is defined based on the percentiles of the normalized residuals $\Delta z_i = \frac{\hat{y}_i - y_i}{1 + y_i}$:

$$\sigma_{68} = \frac{P_{84}(\Delta z) - P_{16}(\Delta z)}{2} \quad (5)$$

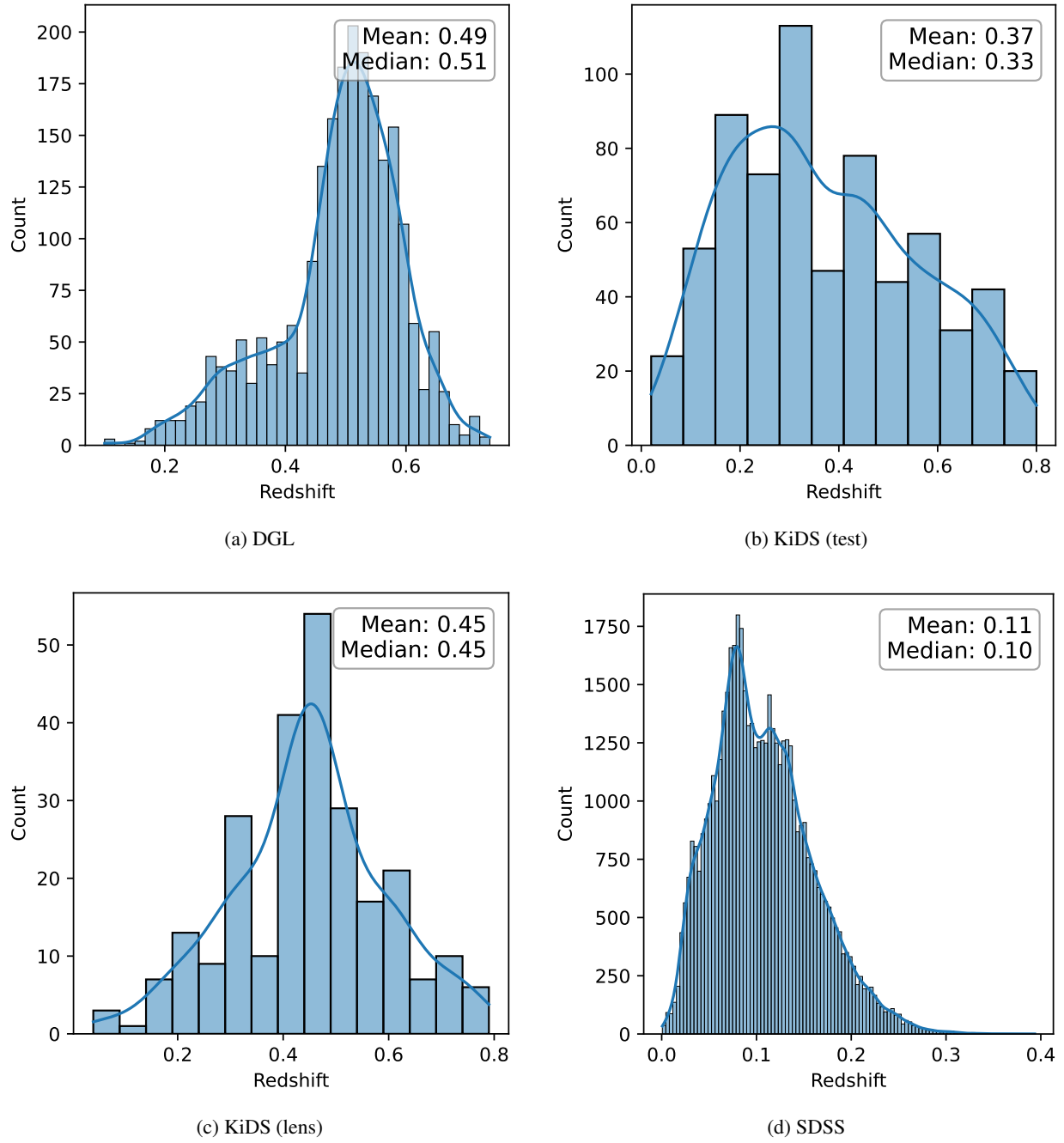


Figure 4: GT redshift distributions for DGL, KiDS and SDSS.

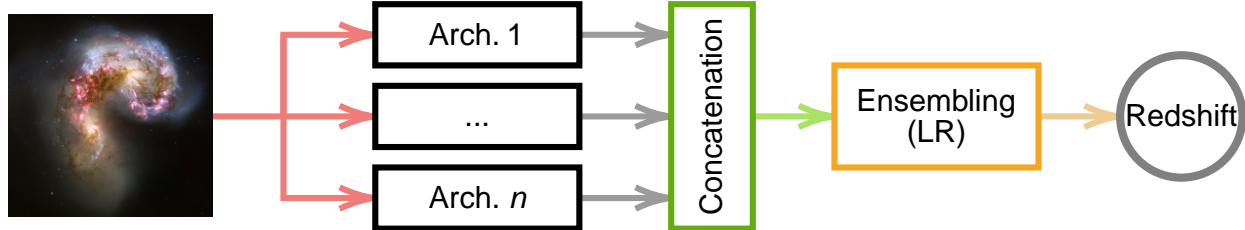


Figure 5: The DeepRed pipeline

where P_{84} and P_{16} are the 84th and 16th percentiles of the distribution of Δz , respectively. Similar to NMAD, σ_{68} provides a robust measure of the dispersion that corresponds to one standard deviation for a normal distribution, ignoring the influence of extreme tails.

The prediction bias is defined as the median of the normalized residuals:

$$\text{Bias} = \text{median} \left(\frac{\hat{y}_i - y_i}{1 + y_i} \right) \quad (6)$$

where y_i is the GT redshift and \hat{y}_i is the predicted value. This metric quantifies the systematic offset of the model predictions. A positive bias indicates a tendency to overestimate the redshift, while a negative bias implies underestimation.

The outlier fraction (η) quantifies the percentage of samples with "catastrophic" prediction errors, defined as:

$$\eta = \frac{1}{N} \sum_{i=1}^N \mathbb{I} \left(\left| \frac{\hat{y}_i - y_i}{1 + y_i} \right| > \theta \right) \quad (7)$$

where \mathbb{I} is the indicator function which equals 1 if the condition is met and 0 otherwise, and θ is the outlier threshold (set to 0.05 in this work). This metric assesses the reliability of the model by tracking the frequency of outliers.

Section 3.4.11 reports which losses and early stopping metrics are used for each dataset.

3.3.1 Uncertainty estimation

Uncertainty estimation allows the identification of significant improvements in metrics for different experiments (see e.g., [26]). In this work, 1σ uncertainties are computed on all the evaluation metrics and are estimated on the test set using bootstrapping, a 4-step statistical technique:

1. Starting from a test set containing D samples (each consisting of a GT label and its associated prediction), create a bootstrap sample b_i by drawing d samples randomly with replacement from the original set.
2. Calculate the desired evaluation metric (e.g., MAE), denoted as m_i , on the resampled set b_i .
3. Repeat steps 1 and 2 a total of k times to generate a collection of k metric values: $\{m_1, m_2, \dots, m_k\}$.
4. Estimate the mean and uncertainty (here reported as $\pm 1\sigma$) from the resulting distribution of metric values.

In this work, the number of data points in the resampled test set is $d = D$ (see also [26]), and the number of bootstrapping iterations is $k = 1000$.

3.4 Pipeline

This work proposes DeepRed, an ML-based pipeline, to estimate the redshift from astronomical images. Figure 5 illustrates the pipeline. First, ML and DL architectures (*Arch. 1* to *Arch. n*) are trained. Then, the estimations of the best architectures are ensembled using a LRE on the best architectures' output latent vectors. The ML and DL architectures belong to different families:

- Feature extraction: this family comprises HOG [48] + SVR¹
- CNN: this family comprises Residual Network (ResNet) [51], EfficientNet [83], A1 [40], A3 [40], NetZ [31] and PhotoZ [72]

¹As implemented in <https://scikit-learn.org/stable/modules/generated/sklearn.svm.SVR.html>.

Table 2: Hyperparameters of the HOG + SVR architecture.

Hyperparameter	Values
Color features	yes, no
Number of orientations (HOG)	8, 16
Explained variance (PCA)	0.6, 0.8, 0.9
ϵ (SVR)	0.1, 0.01

Table 3: Hyperparameters for the ResNet architecture.

Hyperparameter	Values
Embedding size	16, 64, 256
L_2 regularization coefficient	0.01, 0.001, 0.0001
LR	0.01, 0.001, 0.0001
Depth	[2,2,2,2], [3,4,6,3]

- MLP: this family comprises MLPm, a non-convolutional Neural Network (NN) based on Multi-Layer Perceptron (MLP) [84]
- Transformers: this family comprises SwinT [45]

The presented architectures, with the exception of A1, A3, NetZ and PhotoZ, were initially designed for classification. In this work, they are adapted for the regression task by replacing the classification head with a regression head (similar to [85]) formed by a single FC layer.

3.4.1 HOG + SVR

HOG is a CV algorithm designed to capture the edges and shapes of objects in an image. It begins by computing horizontal and vertical gradients using predefined filter kernels, from which the gradient magnitude and orientation are derived for each pixel. The image is then divided into non-overlapping cells (5×5 pixels in this work), and each cell is represented by a histogram of gradient orientations weighted by magnitude. These cells are grouped into blocks. The final image representation is formed by concatenating and normalizing the features of all blocks. To reduce dimensionality and mitigate overfitting, Principal Component Analysis (PCA) is applied to the resulting feature vector [86]. Additional features are obtained by computing the histograms of colours from the original images. The resulting features are given as input to SVR, which is trained to estimate redshift. Table 2 presents the relevant hyperparameters and their values. The other hyperparameters have their default values. "Color features" indicates whether the histograms of colours are retained, "Number of orientations (HOG)" indicates the number of discrete values of the gradient orientations, "Explained variance (PCA)" indicates the minimum required explained variance for PCA and " ϵ (SVR)" defines a margin of tolerance within which prediction errors are not penalized by the loss function. Overall, the experiments consider 24 hyperparameter combinations.

3.4.2 ResNet

ResNet [51] is a DL architecture introduced to improve stability and convergence during training. This architecture has introduced residual blocks, which are the key to stabilization and prevent the problem of vanishing gradients [87]. In residual blocks, the input is directly added to the output of the block through a residual connection. The network² is formed by four stages of residual blocks. The output of the fourth block is given as input to the FC layers, which form the regression head. Table 3 presents the non-default hyperparameters and their values, for a total of 54 hyperparameter combinations. The embedding size indicates the number of dimensions in which the images are represented in the feature space. A small value can make the network unable to learn sufficient information, while a high value could lead to overfitting. The L_2 regularization coefficient controls regularization by adding a penalty to the loss function proportional to the square of the model's parameters. This reduces the risk of overfitting by discouraging large weights. The Learning Rate (LR) determines how much model weights are updated during training: high values may prevent convergence to the global optimum, while overly low values can lead to premature convergence in local minima. The depth hyperparameter defines the number of layers for each stage.

²As implemented in https://huggingface.co/docs/transformers/en/model_doc/resnet (as of July 2025)

Table 4: Details of the EfficientNet architectures B1 to B3 [83]

Architecture	Width Coefficient	Depth Coefficient
B1	1.0	1.1
B2	1.1	1.2
B3	1.2	1.4

Table 5: Hyperparameters for EfficientNet.

Hyperparameter	Values
Dropout	0.3, 0.5
L_2 regularization coefficient	0.01, 0.001, 0.0001
LR	0.01, 0.001, 0.0001
Architecture type	B1, B2, B3

3.4.3 EfficientNet

EfficientNet [83]³ is a CNN-based architecture that uses compound scaling to uniformly scale its dimensions (width, depth, and resolution) with fixed coefficients, rather than scaling each of them separately. Width refers to the number of channels, depth refers to the number of layers, and resolution refers to the size of the input data. In this work, the resolution is fixed and the width and depth scaling parameters are set as in the official Tensorflow implementation⁴. This work uses the architectures from B1 to B3 (detailed in Table 4) as more complex architectures are more prone to overfitting. Table 5 lists the hyperparameters and their corresponding values, showing a total of 54 combinations.

3.4.4 A1

A1 is a CNN designed for regression tasks presented in [40]. It comprises two convolutional layers followed by a PReLU activation and average pooling. The resulting feature map is flattened and passed to three FC layers, each followed by a PReLU activation.

3.4.5 A3

A3 [40] is a CNN architecture designed for regression tasks, incorporating Inception blocks to capture multi-scale features. Its structure includes an initial convolutional layer followed by average pooling, two Inception blocks, another average pooling layer, a third Inception block, a flattening layer, and finally three FC layers.

3.4.6 PhotoZ

PhotoZ [41] is a deep CNN architecture that uses Inception blocks. Its structure includes an initial convolutional layer followed by a sequence of five Inception blocks designed to capture multi-scale spatial features, a flattening layer, and finally multiple FC layers to produce the redshift prediction.

3.4.7 NetZ

NetZ [31] is a CNN architecture designed to estimate photometric redshifts directly from multi-band galaxy images. Its structure comprises a series of convolutional layers for feature extraction, followed by max-pooling layers to reduce spatial dimensions, and FC layers to output the redshift prediction.

3.4.8 MLPm

MLPm [84] is a NN that relies on MLPs to process spatial and channel-wise information instead of using convolutions or attention-based mechanisms. In this architecture, the input image is first divided into non-overlapping patches, which are then converted into vectors and projected into a higher-dimensional space using a linear layer; this process forms the patch embeddings. The main component of the network is the Mixer block, which alternates between two MLPs: one for channel mixing and one for spatial mixing. The channel mixing MLP mixes information across feature channels

³As implemented in https://huggingface.co/docs/transformers/model_doc/efficientnet (as of July 2025)

⁴Available at <https://github.com/tensorflow/tpu/tree/master/models/official/efficientnet> (as of July 2025)

Table 6: Variants of the MLPm architectures [84].

Architecture	Hidden size	Number of layers
S	512	8
B	768	12
L	1024	24

Table 7: Hyperparameters considered for the tuning of the MLPm architecture.

Hyperparameter	Values
LR	0.01, 0.001, 0.0001
L_2 regularization coefficient	0.01, 0.001, 0.0001
Patch size	5, 9
Architecture variant	S, B, L
Dropout	0.0, 0.2

independently for each spatial location. The spatial (or token) mixing MLP, on the other hand, mixes information across feature channels independently for each feature channel. Table 6 summarizes the variants of MLPm (detailed in [84]), and Table 7 presents the hyperparameters and their values, for a total of 108 combinations.

3.4.9 Swin transformer

SwinT is an architecture based on the transformer block. It employs self-attention to capture multi-scale representations of images. Rather than applying attention globally, it partitions the image into patches and groups them into windows. As a result, the model can capture both local and global contextual information. This work uses a window size of 2 patches and a patch size of 5 pixels. The transformer’s 4-layer hierarchical structure is used to look for general information, while the smaller window size allows for the focus on fine-grained local features. The work in [45] shows that the model generalizes better than the original ViT on datasets with fewer samples. For instance, in [88], SwinT has been used for healthcare data. Table 8 shows the architecture variants, and Table 9 shows the hyperparameters’ values, for a total of 162 combinations. In this work, we consider only the architectures with a small number of parameters to prevent overfitting.

3.4.10 Ensembling

Ensembling takes as input the predictions from different base architectures and outputs a new prediction. All possible combinations of 2, 3, and 4 different architectures were tested to identify the best combination for each dataset. The best base models were selected based on their validation set MAE (i.e., for each architecture, we selected the best hyperparameters as the ones associated with the lowest validation MAE).

We use LRE to combine the predictions. This algorithm determines the final prediction by finding a linear combination of the base architectures’ predictions [89], as follows:

$$y = \beta_0 + \sum_{i=1}^N \beta_i x_i \quad (8)$$

where y is the output of the LRE model, β_0 is a constant value, x_i are the outputs of the selected input architectures, β_i are their coefficients and N is the number of selected input architectures. The function is optimized by minimizing the MSE.

Table 8: Architecture variants for SwinT [45].

Architecture	Embedding size	Number of heads	Depth
T	96	[3, 6, 12, 24]	[2, 2, 6, 2]
S	96	[3, 6, 12, 24]	[2, 2, 18, 2]
B	128	[4, 8, 16, 32]	[2, 2, 18, 2]

Table 9: Hyperparameters considered for the tuning of the Swin transformer architecture.

Hyperparameter	Values
Dropout	0.0, 0.2
Encoder stride	3, 5, 9
L_2 regularization coefficient	0.01, 0.001, 0.0001
LR	0.01, 0.001, 0.0001
Architecture variant	T, S, B

3.4.11 Training

The training process of DeepRed is divided into two stages. First, all the architectures are trained separately, using the same inputs. Then LRE, is trained on the outputs of 2 to 4 of the input architectures. Identical data splits are used in both stages to avoid double-dipping.

Table 10: Training and stopping criteria per dataset

Dataset	Loss function	Max epochs	Early stopping	
			Patience	Metrics
DGL	MSE	500	100	R^2
KiDS	MSE	500	100	R^2
SDSS	MAE	100	20	MAE

Table 10 reports the loss function, maximum number of epochs and early stopping parameters for all the datasets. All the input architectures for DGL and KiDS are trained for 500 epochs with early stopping on the R^2 (which, different from MAE and MSE, is scale-invariant and is a direct indicator of the model’s explanatory power) and a patience of 100 epochs, similar to [26]. For each dataset, the best model is the one with the best MAE on the validation set. For the SDSS dataset, all architectures are trained for 100 epochs (consistently with [40]) with a patience of 20. MAE is used for both the loss function and early stopping in DeepRed DL architectures, as it outperforms the combination of MSE for the loss and R^2 for early stopping (see also subsection 4.3). The best hyperparameters for each network are chosen based on the validation set and tested on a lockbox test set. The best architecture-hyperparameter combinations are also chosen on the validation set and tested on the same lockbox test set.

3.5 Explainability with SHAP

SHAP is a game-theoretic approach used to explain ML models predictions. When applied to images, it identifies the regions of the images that contribute most significantly to the model’s predictions.

The work in [90] provides a summary of the algorithm for image analysis. SHAP relies on a masker to hide portions of the images. In this work, the masker blurs patches of the image using a 5×5 pixels kernel. The pre-trained regression model used for estimating the redshift is then applied to the masked images, and the SHAP value is computed for each masked region i as follows:

$$\phi_i = \sum_{S \subseteq N \setminus \{i\}} \frac{|S|! (|N| - |S| - 1)!}{|N|!} [f(S \cup \{i\}) - f(S)] \quad (9)$$

where ϕ_i is the SHAP value for region i , S is a subset of regions that does not include i , N is the complete set of features (or regions), $f(S)$ is the result of the model with the region i blurred, $f(S \cup \{i\})$ is the result of the model considering S plus the region i not blurred and $\frac{|S|! (|N| - |S| - 1)!}{|N|!}$ is the weight that normalizes the contribution of i based on the size of S .

Finally, the SHAP values (ϕ_i) of each region are aggregated to provide a heatmap for each image. In this work, the most influential regions are those with the highest absolute values of the SHAP coefficients ($|\phi_i|$).

Table 11: MAE on the test set for each dataset in DGL. All numerical results are rounded to the third decimal place for consistency. The best results, and those falling within their confidence intervals, are highlighted in bold.

Network	DES-deep	DES-wide	DESI-DOT	LSST-wide
HOG + SVR	0.067 ± 0.001	0.045 ± 0.001	0.052 ± 0.001	0.048 ± 0.001
A1	0.064 ± 0.001	0.024 ± 0.000	0.029 ± 0.001	0.027 ± 0.001
A3	0.061 ± 0.001	0.033 ± 0.001	0.037 ± 0.001	0.036 ± 0.001
NetZ	0.064 ± 0.001	0.023 ± 0.001	0.027 ± 0.001	0.025 ± 0.001
PhotoZ	0.061 ± 0.001	0.013 ± 0.000	0.020 ± 0.001	0.016 ± 0.000
EfficientNet	0.034 ± 0.001	0.013 ± 0.000	0.016 ± 0.000	0.014 ± 0.000
MLPm	0.053 ± 0.001	0.010 ± 0.000	0.015 ± 0.000	0.013 ± 0.000
ResNet	0.069 ± 0.001	0.010 ± 0.000	0.017 ± 0.000	0.016 ± 0.000
SwinT	0.045 ± 0.001	0.010 ± 0.000	0.014 ± 0.000	0.012 ± 0.000
Ensemble	0.034 ± 0.001	0.009 ± 0.000	0.012 ± 0.000	0.011 ± 0.000
Improvement [%]	45	36	38	32

Table 12: NMAD on the test set for each dataset in DGL. All numerical results are rounded to the third decimal place for consistency. The best results, and those falling within their confidence intervals, are highlighted in bold.

Network	DES-deep	DES-wide	DESI-DOT	LSST-wide
HOG + SVR	0.051 ± 0.002	0.037 ± 0.001	0.040 ± 0.001	0.036 ± 0.001
A1	0.051 ± 0.001	0.017 ± 0.000	0.022 ± 0.001	0.020 ± 0.001
A3	0.048 ± 0.001	0.027 ± 0.001	0.029 ± 0.001	0.027 ± 0.001
NetZ	0.051 ± 0.001	0.016 ± 0.000	0.021 ± 0.001	0.018 ± 0.000
PhotoZ	0.048 ± 0.002	0.007 ± 0.000	0.011 ± 0.000	0.009 ± 0.000
EfficientNet	0.021 ± 0.001	0.010 ± 0.000	0.009 ± 0.000	0.009 ± 0.000
MLPm	0.039 ± 0.001	0.004 ± 0.000	0.006 ± 0.000	0.005 ± 0.000
ResNet	0.054 ± 0.001	0.005 ± 0.000	0.009 ± 0.000	0.009 ± 0.000
SwinT	0.032 ± 0.001	0.005 ± 0.000	0.007 ± 0.000	0.008 ± 0.000
Ensemble	0.023 ± 0.001	0.003 ± 0.000	0.005 ± 0.000	0.005 ± 0.000
Improvement [%]	55	51	52	46

4 Evaluation

This section reports the quantitative and qualitative evaluation of DeepRed on the datasets introduced in subsection 3.1. For each result, uncertainty is reported as presented in subsubsection 3.3.1. In this work, DeepRed architectures (ResNet, MLPm, SwinT, EfficientNet and ensembling) are compared with baseline architectures (HOG + SVR, A1, A3, NetZ and PhotoZ). The DL baseline architectures are those presented in [40, 31, 41], and HOG + SVR is a ML baseline.

4.1 DeepGraviLens

Table 11 summarizes the results in terms of MAE and shows that the choice of the architecture is determinant. HOG + SVR, a simple architecture, is able to exploit some shape information to estimate redshift, but is significantly worse than all the DL architectures. State-of-the-art DL algorithms and ensembling yields substantial improvements (32% to 45%) over baseline DL architectures (A1, A3, NetZ and PhotoZ) and HOG + SVR. Overall, non-ensembled algorithms already outperform the baselines, while ensembling improves performance further or matches that of the best individual architecture (e.g., DES-deep). The worst architecture among those presented in this work is ResNet. Overall, while ensembling is the best method on all the datasets, results change significantly based on the datasets' characteristics, as also shown in [26]. DES-deep is the most challenging dataset, leading to higher MAE. Moreover, the architectures presented in this work achieve a larger improvement in MAE over the best baseline architecture ($\approx 45\%$) compared with other datasets ($\approx 35\%$), suggesting that for more noisy datasets the features extracted by deep architectures are more relevant than in higher-quality datasets.

Table 13: σ_{68} on the test set for each dataset in DGL. All numerical results are rounded to the third decimal place for consistency. The best results, and those falling within their confidence intervals, are highlighted in bold.

	DES-deep	DES-wide	DESI-DOT	LSST-wide
HOG + SVR	0.054 ± 0.001	0.036 ± 0.001	0.041 ± 0.001	0.038 ± 0.001
A1	0.052 ± 0.001	0.018 ± 0.000	0.022 ± 0.001	0.021 ± 0.001
A3	0.049 ± 0.001	0.026 ± 0.000	0.029 ± 0.001	0.028 ± 0.001
NetZ	0.051 ± 0.001	0.017 ± 0.000	0.021 ± 0.000	0.019 ± 0.000
PhotoZ	0.048 ± 0.001	0.008 ± 0.000	0.012 ± 0.000	0.010 ± 0.000
EfficientNet	0.024 ± 0.001	0.008 ± 0.000	0.010 ± 0.000	0.009 ± 0.000
MLPm	0.040 ± 0.001	0.005 ± 0.000	0.007 ± 0.000	0.006 ± 0.000
ResNet	0.054 ± 0.001	0.006 ± 0.000	0.011 ± 0.000	0.010 ± 0.000
SwinT	0.035 ± 0.001	0.005 ± 0.000	0.008 ± 0.000	0.008 ± 0.000
Ensemble	0.026 ± 0.001	0.004 ± 0.000	0.007 ± 0.000	0.006 ± 0.000
Improvement [%]	50	49	45	43

Table 14: Bias on the test set for each dataset in DGL. All numerical results are rounded to the third decimal place for consistency. The best results, and those falling within their confidence intervals, are highlighted in bold.

	DES-deep	DES-wide	DESI-DOT	LSST-wide
HOG + SVR	-0.002 ± 0.001	0.000 ± 0.001	0.000 ± 0.001	0.000 ± 0.001
A1	-0.002 ± 0.001	-0.000 ± 0.000	-0.003 ± 0.001	-0.001 ± 0.000
A3	-0.004 ± 0.001	-0.003 ± 0.001	-0.002 ± 0.001	-0.002 ± 0.001
NetZ	-0.009 ± 0.001	-0.001 ± 0.000	-0.002 ± 0.001	-0.003 ± 0.000
PhotoZ	-0.009 ± 0.001	0.001 ± 0.000	0.000 ± 0.000	0.000 ± 0.000
EfficientNet	0.001 ± 0.000	0.001 ± 0.000	0.001 ± 0.000	0.000 ± 0.000
MLPm	0.001 ± 0.001	-0.001 ± 0.000	-0.002 ± 0.000	0.000 ± 0.000
ResNet	-0.011 ± 0.001	0.001 ± 0.000	0.001 ± 0.000	-0.005 ± 0.000
SwinT	-0.001 ± 0.001	0.000 ± 0.000	0.000 ± 0.000	0.001 ± 0.000
Ensemble	-0.000 ± 0.001	-0.000 ± 0.000	0.000 ± 0.000	-0.000 ± 0.000

Table 15: Outlier rate on the test set for each dataset in DGL. All numerical results are rounded to the third decimal place for consistency. The best results, and those falling within their confidence intervals, are highlighted in bold.

	DES-deep	DES-wide	DESI-DOT	LSST-wide
HOG + SVR	0.354 ± 0.010	0.182 ± 0.008	0.232 ± 0.009	0.203 ± 0.009
A1	0.335 ± 0.010	0.040 ± 0.004	0.060 ± 0.005	0.056 ± 0.005
A3	0.307 ± 0.010	0.096 ± 0.006	0.109 ± 0.006	0.102 ± 0.007
NetZ	0.341 ± 0.010	0.036 ± 0.004	0.045 ± 0.004	0.044 ± 0.004
PhotoZ	0.319 ± 0.010	0.017 ± 0.003	0.041 ± 0.004	0.032 ± 0.004
EfficientNet	0.114 ± 0.007	0.018 ± 0.003	0.025 ± 0.003	0.021 ± 0.003
MLPm	0.253 ± 0.009	0.020 ± 0.003	0.042 ± 0.004	0.036 ± 0.004
ResNet	0.368 ± 0.010	0.013 ± 0.002	0.031 ± 0.004	0.027 ± 0.003
SwinT	0.194 ± 0.008	0.017 ± 0.003	0.025 ± 0.003	0.021 ± 0.003
Ensemble	0.111 ± 0.007	0.009 ± 0.002	0.019 ± 0.003	0.012 ± 0.002
Improvement [%]	64	48	54	61

The better results of the DeepRed DL algorithms presented in this work are also observed when comparing the R^2 scores. In DES-deep, the DeepRed DL algorithms have, on average, $R^2 \approx 0.60$, compared with $R^2 \approx 0.31$ of HOG + SVR and $R^2 \approx 0.38$ for the five baseline architectures. In DES-wide, $R^2 \approx 0.97$ for the DeepRed DL architectures, compared to an average of ≈ 0.85 for the baseline architectures. In DESI-DOT, the DeepRed architectures have $R^2 \approx 0.94$, compared to an average of $R^2 \approx 0.80$ for the baseline algorithms. In LSST, $R^2 \approx 0.95$ for the DeepRed architectures, compared to an average baseline of $R^2 \approx 0.82$.

Similar conclusions can be drawn from Table 12 and Table 13, which report the NMAD and σ_{68} dispersion metrics, respectively. They confirm the superiority of the proposed DL architectures. MLPm and ensembling consistently achieve the lowest dispersion across the DES-wide, DESI-DOT, and LSST-wide datasets. Notably, on the challenging DES-deep dataset, EfficientNet has the lowest scatter ($\sigma_{68} \approx 0.024$ and NMAD ≈ 0.021), outperforming ensembling slightly. The improvements in scatter reduction are substantial (46% to 55% for NMAD and 43% to 50% for σ_{68}) compared to the best baseline methods. A paired bootstrap test (16th–84th percentile confidence interval) on NMAD confirms a statistically significant improvement of our best architecture over the baselines.

Table 14 shows that the bias is negligible for the majority of the architectures and datasets. The DL models presented in this work mitigate systematic offsets, achieving bias values of ≈ 0 across all datasets. While the baseline DL models (e.g., NetZ, PhotoZ) and HOG + SVR occasionally lead to small biases (up to -0.009 in DES-deep), the proposed architectures are on average less biased.

Finally, Table 15 highlights the significant reduction in the outlier rate. On the higher-quality datasets (DES-wide, DESI-DOT, LSST-wide), the proposed architectures remove most of the catastrophic failures, achieving an outlier rate $< 2\%$. Even on the more challenging DES-deep dataset, the outlier rate is reduced by $\approx 64\%$ compared to the baselines, achieving $\approx 11\%$ for ensembling and EfficientNet. These improvements further demonstrate the robustness of the proposed models.

4.1.1 Explainability

Figures 6, 7, 8, and 9 show representative examples of SHAP heatmaps for lensing systems in DGL, obtained from the best non-ensembled models. In each image, the yellow dot indicates the position of the region associated with the highest absolute SHAP value. DES-deep is the most challenging dataset due to the noisy background, so SHAP assigns high importance to multiple regions, reflecting uncertainty in identifying the features determining redshift. In contrast, DES-wide shows a more localised SHAP heatmap, concentrated on the lensing system, where the model is focusing. The DESI-DOT example exhibits a sharp peak, implying that the model relies almost exclusively on the lensing object and not on the Einstein ring or the background. Lastly, in LSST-wide, the influential regions are more spread, indicating that the model uses both the lens and the background objects to estimate redshift.

To assess the ability of the model to focus on the most relevant areas, we calculate the distance between the most influential region and the centre of the image (where the object of interest is also centred). Each distance is normalized between 0 and 1. Figure 10 shows the distribution of the distances for the four datasets. The mean distance for DES-deep is 0.474 (median 0.598), indicating that the model’s focus diverges significantly from the lensing region and that the lens spreads over the image. In contrast, the distances are significantly lower for LSST-wide (mean 0.090, median 0.050), DESI-DOT (mean 0.068, median 0.050), and DES-wide (mean 0.054, median 0.022), confirming that the model typically concentrates its attention near the lens centre. This trend suggests that higher image quality leads to more interpretable behaviour, improving trustworthiness in the redshift estimation models. Table 16 reports the localization accuracy for the DGL datasets. As observed in distances distribution, the most challenging dataset is DES-deep, with a localization accuracy of $\approx 38\%$, while the localization accuracy is $> 95\%$ for the other DGL datasets.

The nature of KiDS targets introduces a challenge regarding the reliability of GT labels (i.e., photometric redshifts derived from a broader set of spectral channels than the four bands available to the DeepRed models). This discrepancy creates an information gap, as the targets contain information that is absent in the input images. As a consequence, the ML algorithms estimate redshift but also approximate the outputs of a higher-dimensional estimator using limited photometric data. This reliance on estimated targets introduces label noise, but it also imposes a pessimistic performance ceiling compared to the higher-dimensional case, which contains more information. The proposed architectures achieve low bias and good performance across different metrics despite the information deficit, which demonstrates their capability to extract robust features even from limited observational data.

4.2 KiDS

Table 17 summarizes the results of the proposed architectures in terms of MAE. As in the case of DGL, deep architectures outperform HOG + SVR, indicating that shape-based information is not sufficient for accurate redshift estimation. In general, state-of-the-art architectures outperform simpler baseline architectures such as A1, A3, PhotoZ

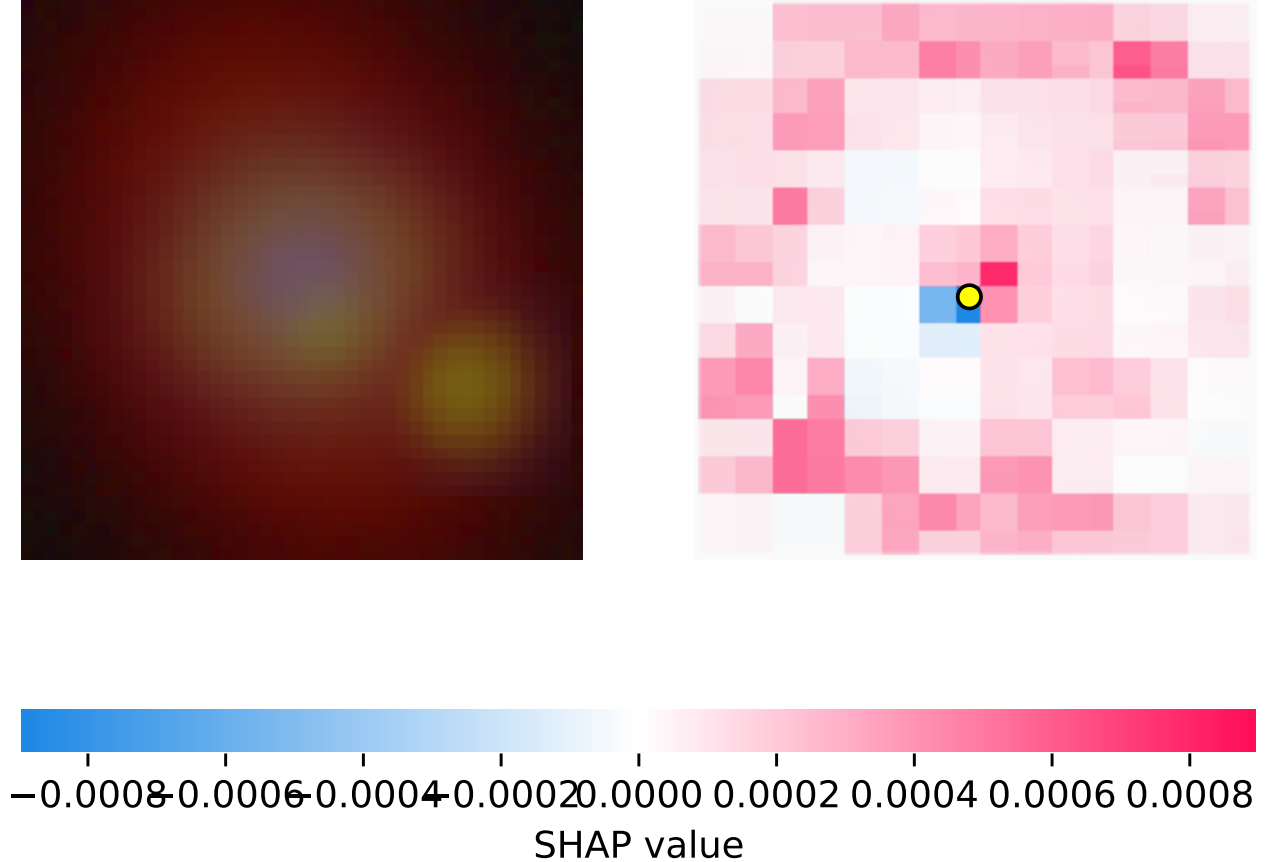


Figure 6: Example of SHAP heatmap on the DES-deep dataset. The yellow dot indicates the position of the most influential pixel according to SHAP. Each side corresponds to ≈ 12 arcsec.

Table 16: Localization accuracy for the DGL datasets.

Dataset	Bounding Box Size (%)	Localization Accuracy (%)
DES-deep	17.00	38.08
DES-wide	18.00	99.07
DESI-DOT	18.19	97.92
LSST-wide	19.01	95.11

and NetZ, and ensembling is, for most of the metrics, as effective or more effective than individual architectures. Its effectiveness is observed consistently in the two subsets (where "test" refers to the lower-probability candidate lenses and "lens" to the high-probability lenses, as presented in subsubsection 3.1.2). Both SwinT and MLPm, which are not based on CNNs, outperform the other architectures. Still, MAE is higher than on DGL data, suggesting that the noise in real data makes estimations more difficult. Furthermore, the best MAE (> 0.06) is greater than the error introduced by the use of photometric redshift in place of spectroscopic redshift (≈ 0.01) presented in [91]. For this reason, the reported improvements reflect an improvement in the model's ability to estimate redshift, rather than overfitting to label noise. Overall, the resulting MAE can be regarded as an upper bound of the error, given by the error introduced by GT photometric redshift and the estimation error introduced by the network.

As in the case of the simulated datasets, the better results of the DeepRed DL algorithms are also observed when comparing the R^2 score. For the test dataset, $R^2 \approx 0.72$, compared with $R^2 \approx 0.61$ for the baseline architectures. For high-probability lenses, $R^2 \approx 0.62$ for the new architectures, compared with $R^2 \approx 0.45$ for the baseline ones. In this case, the result is more informative than MAE alone, as the distribution of the redshifts is different between the two subsets, and high-probability lenses tend to have a higher redshift in this dataset.

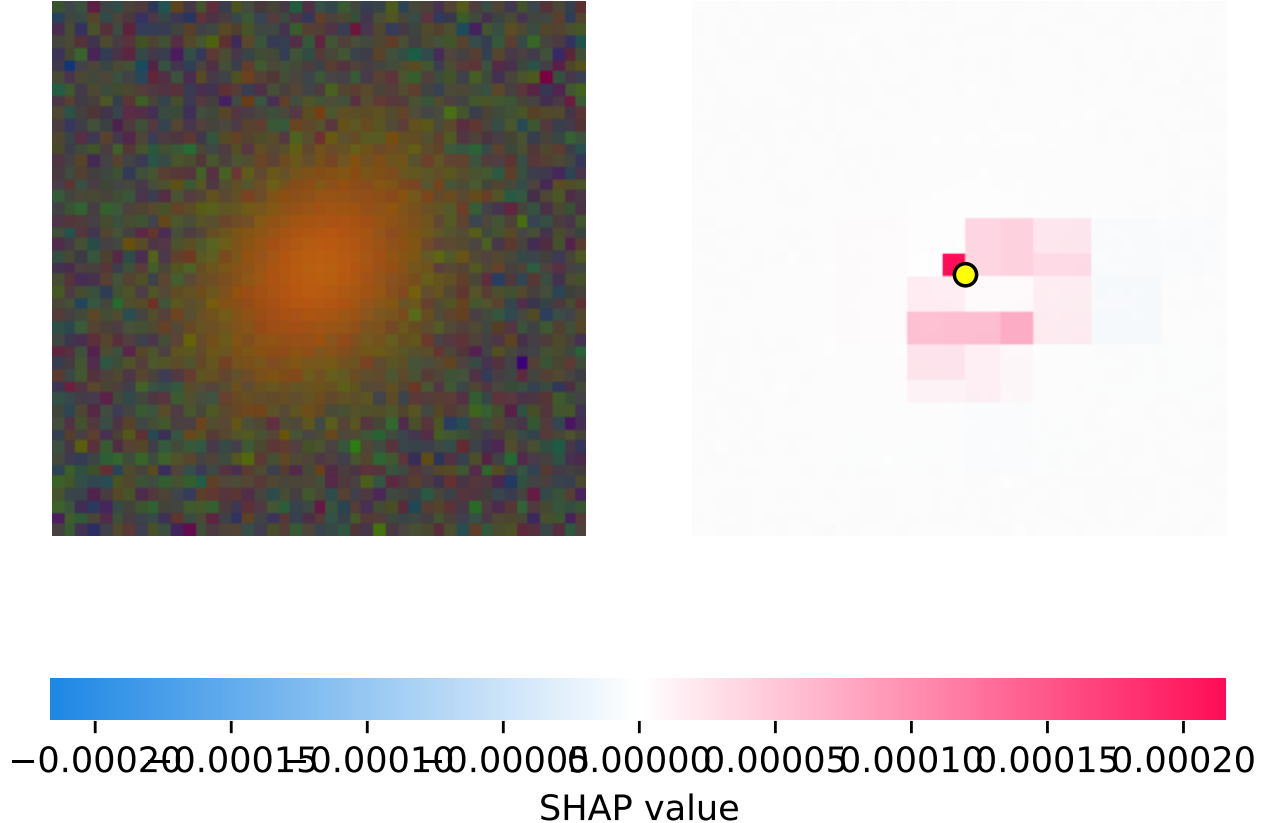


Figure 7: Example of SHAP heatmap on the DES-wide dataset. The yellow dot indicates the position of the most influential pixel according to SHAP. Each side corresponds to ≈ 12 arcsec.

Table 18 and Table 19 present the results for the dispersion metrics NMAD and σ_{68} , respectively. The proposed DL architectures consistently achieve lower scatter compared to the baselines on both the "lens" and "test" subsets. Ensembling, SwinT and MLPm perform particularly well on average. The improvement in scatter reduction is significant, reaching up to 27% for NMAD and 17% for σ_{68} compared to the best baseline models. While the absolute values are higher than those in the simulated DGL datasets, this is expected given the higher noise levels in real data. A paired bootstrap test (16th–84th percentile confidence interval) on NMAD confirms a statistically significant improvement of our best architecture over the baselines.

Table 20 shows that the proposed architectures mitigate bias. Ensembling, EfficientNet, MLPm, ResNet, and SwinT all achieve low bias values. In contrast, some baseline models, such as A1 and PhotoZ, lead to small but non-negligible biases, especially on the lens set (up to 0.017). This confirms the robustness of the proposed methods in producing unbiased estimates even on real observational data.

Finally, Table 21 highlights the reduction in outliers. The outlier rate is significantly improved by the proposed architectures, with Ensembling achieving the lowest rate on both the lens set (≈ 0.296) and the test set (≈ 0.289). This represents an improvement of up to $\approx 16\%$ compared to the best baselines. Although the outlier rates are higher than in the simulated data, the relative improvement demonstrates the capability of these models to handle real observations better than existing methods.

4.2.1 Explainability

Figures 11, 12, 13, and 14 show representative examples of SHAP heatmaps for images in KiDS, obtained from the best non-ensembled models. In each image, the yellow dot indicates the pixel with the highest absolute SHAP value (i.e., the most influential region for the model's estimate). Low-probability lens images (Figures 11, 12) are associated with SHAP heatmaps that exhibit low-magnitude values dispersed around regions near the centre, suggesting more uncertainty in the most relevant region for redshift estimation. In contrast, Figures 13 and 14 correspond to high-probability lens candidates, and SHAP heatmaps are more concentrated near the image centers.

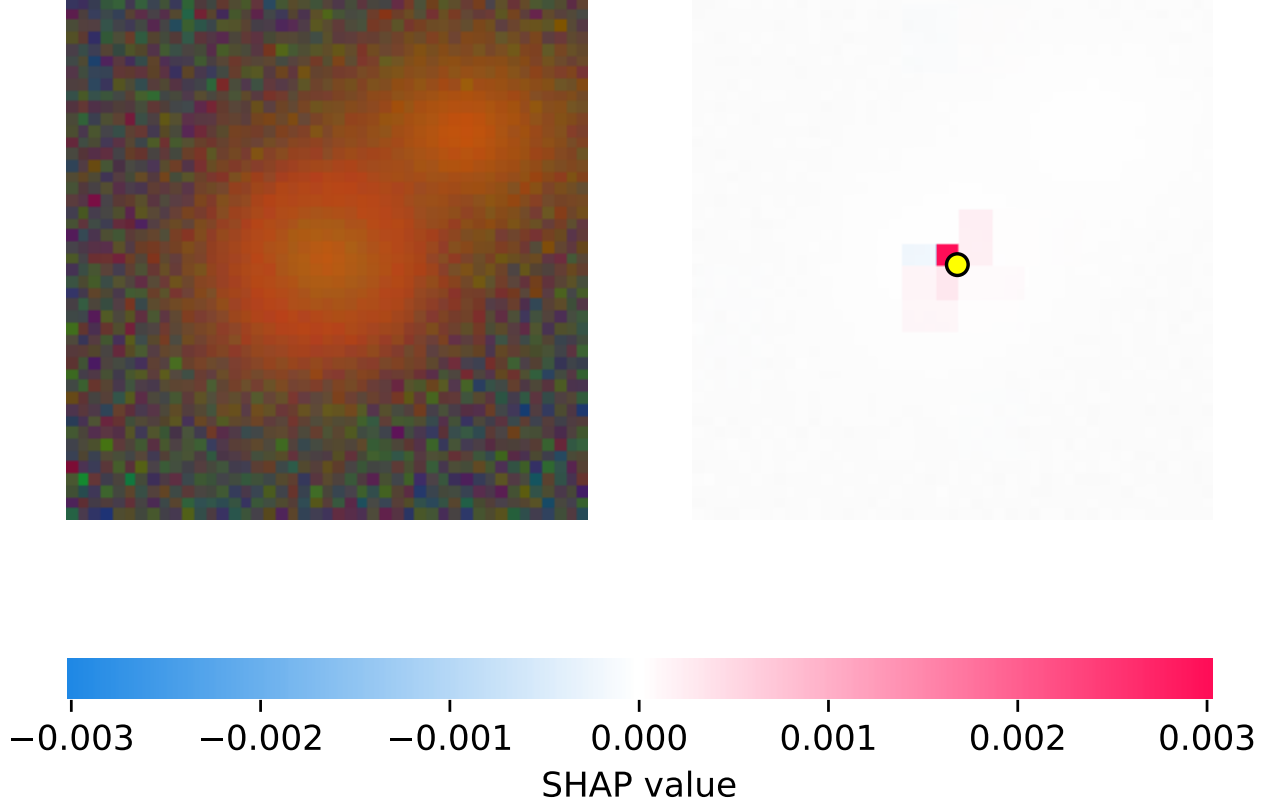


Figure 8: Example of SHAP heatmap on the DESI-DOT dataset. The yellow dot indicates the position of the most influential pixel according to SHAP. Each side corresponds to ≈ 12 arcsec.

Table 17: MAE of the models trained on the KiDS dataset. The results are taken on the test set and lens set for the models with the combination of hyperparameters with the best performance on the validation set. All numerical results are rounded to the third decimal place for consistency. The best results, and those falling within their confidence intervals, are highlighted in bold.

Network	KiDS (lens)	KiDS (test)
HOG + SVR	0.108 ± 0.006	0.114 ± 0.004
A1	0.072 ± 0.004	0.072 ± 0.003
A3	0.073 ± 0.004	0.077 ± 0.003
NetZ	0.069 ± 0.004	0.069 ± 0.003
PhotoZ	0.070 ± 0.004	0.071 ± 0.003
EfficientNet	0.077 ± 0.004	0.068 ± 0.003
MLPm	$\mathbf{0.064 \pm 0.004}$	$\mathbf{0.066 \pm 0.003}$
ResNet	0.066 ± 0.005	0.071 ± 0.003
SwinT	$\mathbf{0.064 \pm 0.004}$	0.067 ± 0.003
Ensemble	$\mathbf{0.060 \pm 0.004}$	$\mathbf{0.063 \pm 0.003}$
Improvement [%]	14	10

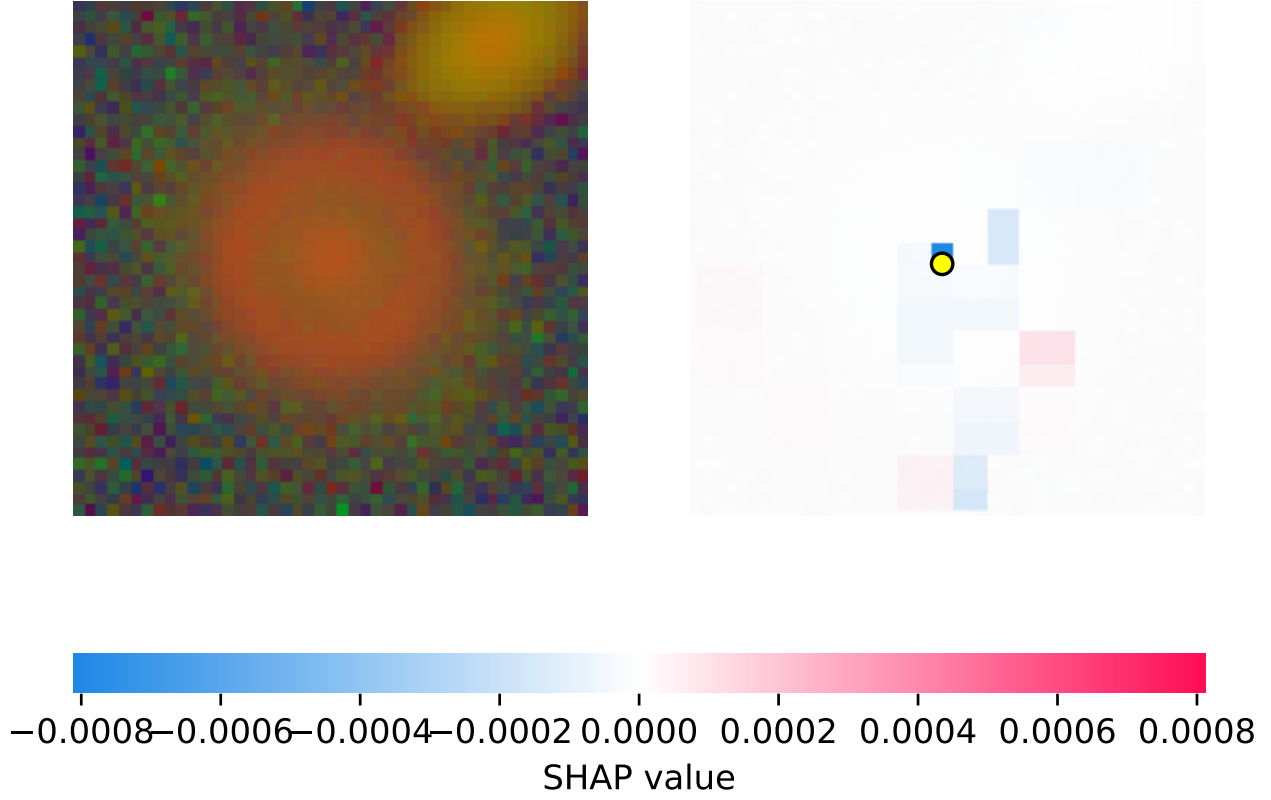


Figure 9: Example of SHAP heatmap on the LSST-wide dataset. The yellow dot indicates the position of the most influential pixel according to SHAP. Each side corresponds to ≈ 9 arcsec.

Table 18: NMAD of the models trained on the KiDS dataset. The results are taken on the test set and lens set for the models with the combination of hyperparameters with the best performance on the validation set. All numerical results are rounded to the third decimal place for consistency. The best results, and those falling within their confidence intervals, are highlighted in bold.

	KiDS (lens)	KiDS (test)
HOG + SVR	0.081 ± 0.006	0.088 ± 0.005
A1	0.051 ± 0.004	0.049 ± 0.003
A3	0.051 ± 0.005	0.054 ± 0.004
NetZ	0.049 ± 0.004	0.046 ± 0.003
PhotoZ	0.052 ± 0.004	0.049 ± 0.002
EfficientNet	0.052 ± 0.004	0.046 ± 0.003
MLPm	0.041 ± 0.003	0.044 ± 0.002
ResNet	0.040 ± 0.004	0.050 ± 0.002
SwinT	0.042 ± 0.004	0.043 ± 0.002
Ensemble	0.036 ± 0.004	0.039 ± 0.002
Improvement [%]	27	16

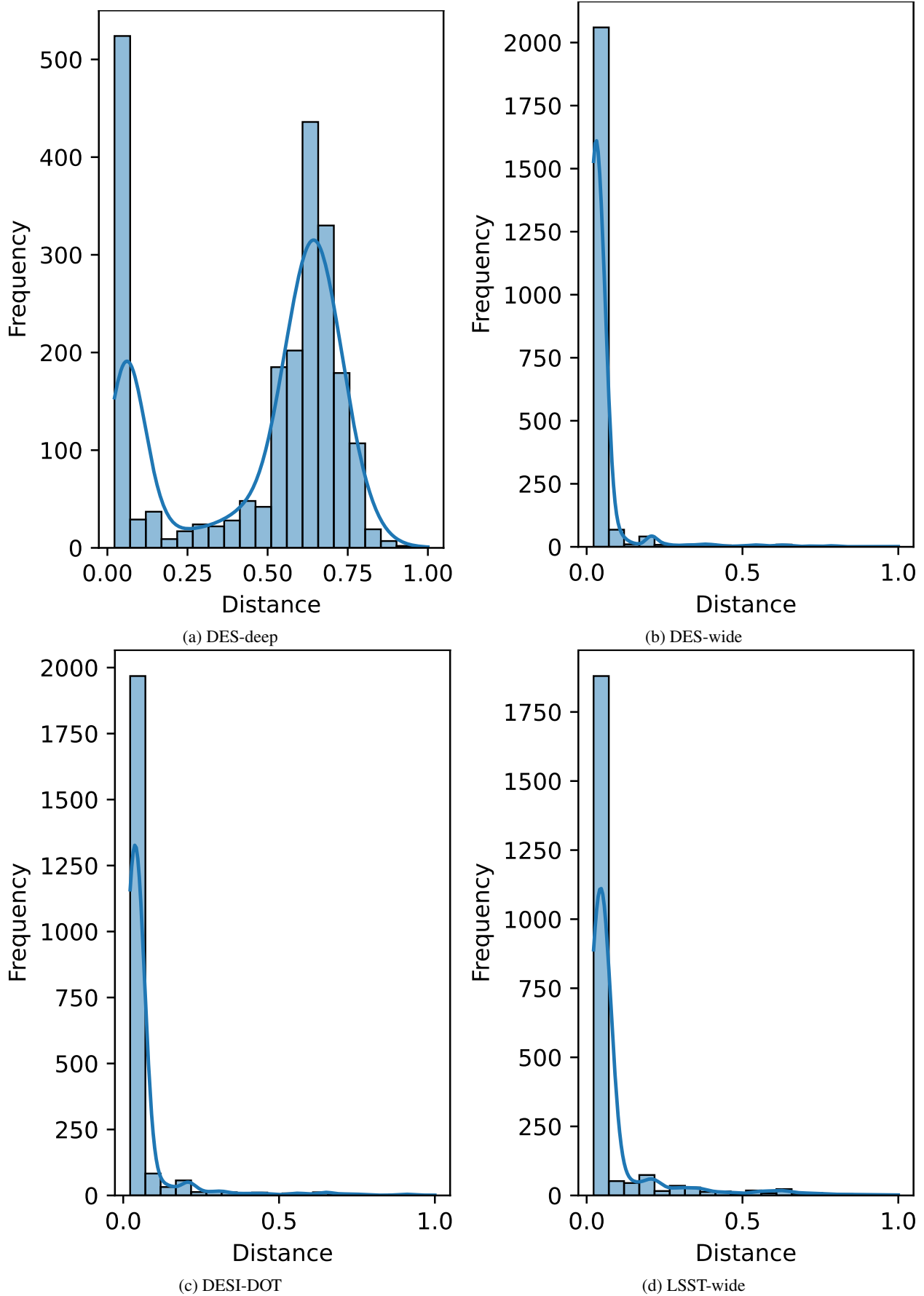


Figure 10: Distribution of the distances between the most influential pixels and the centres of the images for the four DGL dataset. The distances range between 0 and 1, where 1 indicates the maximum possible distance in a single image. ²²

Table 19: σ_{68} of the models trained on the KiDS dataset. The results are taken on the test set and lens set for the models with the combination of hyperparameters with the best performance on the validation set. All numerical results are rounded to the third decimal place for consistency. The best results, and those falling within their confidence intervals, are highlighted in bold.

	KiDS (lens)	KiDS (test)
HOG + SVR	0.078 ± 0.007	0.096 ± 0.004
A1	0.054 ± 0.004	0.057 ± 0.003
A3	0.058 ± 0.005	0.061 ± 0.003
NetZ	0.051 ± 0.004	0.055 ± 0.003
PhotoZ	0.054 ± 0.005	0.054 ± 0.004
EfficientNet	0.050 ± 0.005	0.051 ± 0.003
MLPm	0.049 ± 0.003	0.049 ± 0.003
ResNet	0.050 ± 0.004	0.054 ± 0.003
SwinT	0.049 ± 0.005	0.048 ± 0.003
Ensemble	0.045 ± 0.005	0.045 ± 0.003
Improvement [%]	13	17

Table 20: Bias of the models trained on the KiDS dataset. The results are taken on the test set and lens set for the models with the combination of hyperparameters with the best performance on the validation set. All numerical results are rounded to the third decimal place for consistency. The best results, and those falling within their confidence intervals, are highlighted in bold.

	KiDS (lens)	KiDS (test)
HOG + SVR	-0.010 ± 0.007	0.000 ± 0.004
A1	0.017 ± 0.004	0.002 ± 0.002
A3	0.014 ± 0.003	0.004 ± 0.003
NetZ	-0.010 ± 0.003	0.004 ± 0.002
PhotoZ	0.015 ± 0.003	0.004 ± 0.002
EfficientNet	-0.024 ± 0.002	-0.007 ± 0.002
MLPm	0.002 ± 0.004	-0.004 ± 0.002
ResNet	-0.001 ± 0.003	0.006 ± 0.002
SwinT	-0.011 ± 0.003	-0.001 ± 0.002
Ensemble	-0.004 ± 0.003	-0.000 ± 0.002

Table 21: Outlier rate of the models trained on the KiDS dataset. The results are taken on the test set and lens set for the models with the combination of hyperparameters with the best performance on the validation set. All numerical results are rounded to the third decimal place for consistency. The best results, and those falling within their confidence intervals, are highlighted in bold.

	KiDS (lens)	KiDS (test)
HOG + SVR	0.539 ± 0.031	0.556 ± 0.019
A1	0.379 ± 0.031	0.359 ± 0.019
A3	0.387 ± 0.031	0.395 ± 0.019
NetZ	0.333 ± 0.029	0.349 ± 0.019
PhotoZ	0.355 ± 0.030	0.343 ± 0.019
EfficientNet	0.399 ± 0.031	0.331 ± 0.019
MLPm	0.323 ± 0.029	0.319 ± 0.018
ResNet	0.330 ± 0.030	0.331 ± 0.018
SwinT	0.332 ± 0.029	0.310 ± 0.018
Ensemble	0.296 ± 0.028	0.289 ± 0.018
Improvement [%]	11	16

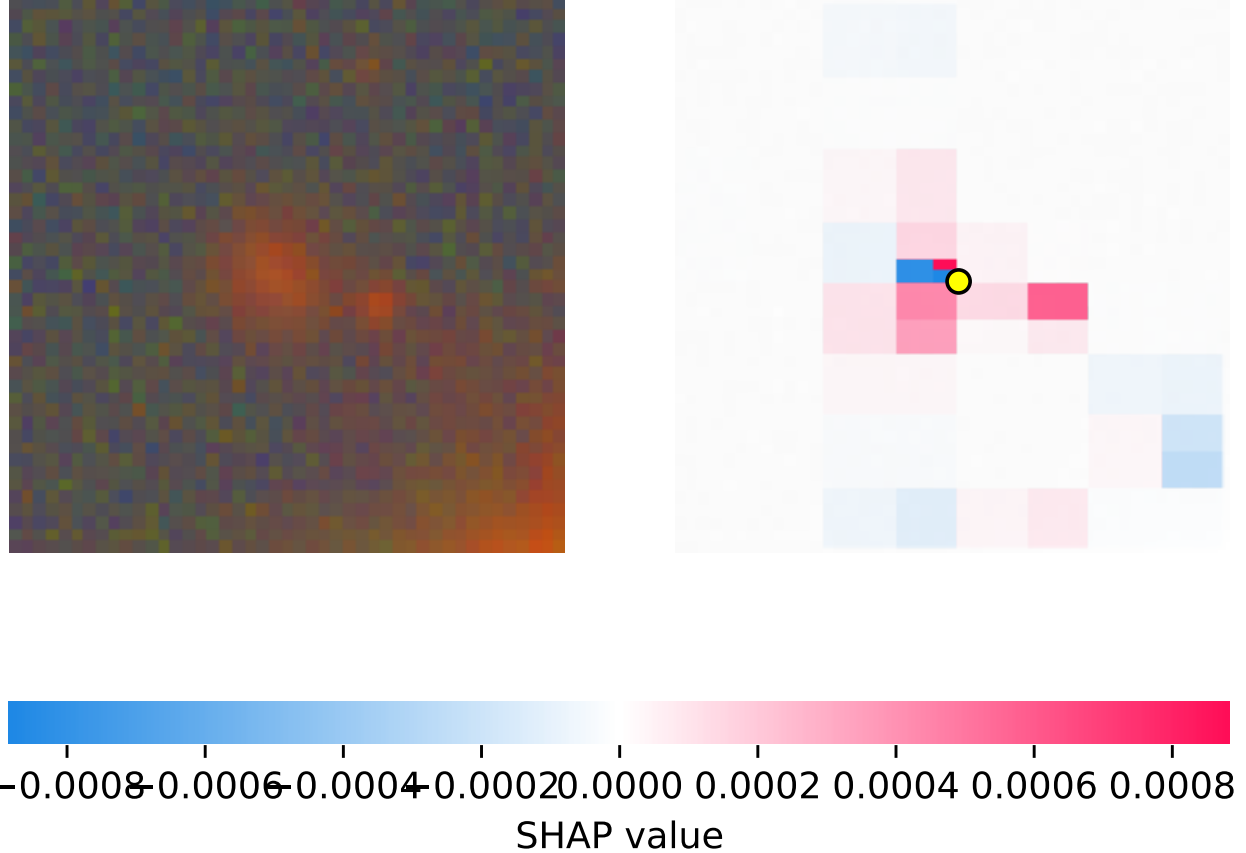


Figure 11: Example of a SHAP heatmap on the KiDS dataset (test). The yellow dot indicates the position of the most influential pixel according to SHAP. Each side corresponds to ≈ 9 arcsec.

To quantify the relevance of the most influential pixels, Figure 15 shows the distribution of their distances from the image centre (normalised between 0 and 1), across the entire dataset. In the low-probability (test) subset, the mean distance is 0.048 and the median distance is 0.022, while on the high-probability (lens) subset, the mean distance is 0.033 and the median distance is 0.022, further underlying the ability of the models to focus on the objects particularly in the case of high-probability lenses.

Table 22: Localization accuracy for the KiDS dataset.

Dataset	Bounding Box Size (%)	Localization Accuracy (%)
KiDS (test)	54.31	97.76
KiDS (lens)	68.96	99.61

Table 22 reports the localization accuracy for the KiDS dataset. In this case, bounding boxes are generally bigger than those in DGL, with the lens subset having bigger bounding boxes because of the magnification introduced by the candidate lens. Localization accuracy is comparable to that of DGL ($> 97\%$), with no significant differences in the two KiDS subsets.

4.3 SDSS

Table 23 reports the MAE on the SDSS dataset for all models, using the test set for evaluation and selecting the best-performing hyperparameter configurations from the KiDS test set. Across all models, the MLPm architecture achieves the best individual performance with an MAE of 0.011, similar to A3 and A1 with scores of 0.012 and 0.013, respectively. HOG + SVR, a traditional feature-based approach, is less effective than other algorithms and has a MAE of 0.055, which is 5 times higher than the best-performing deep learning model. LRE has a MAE of 0.013, slightly

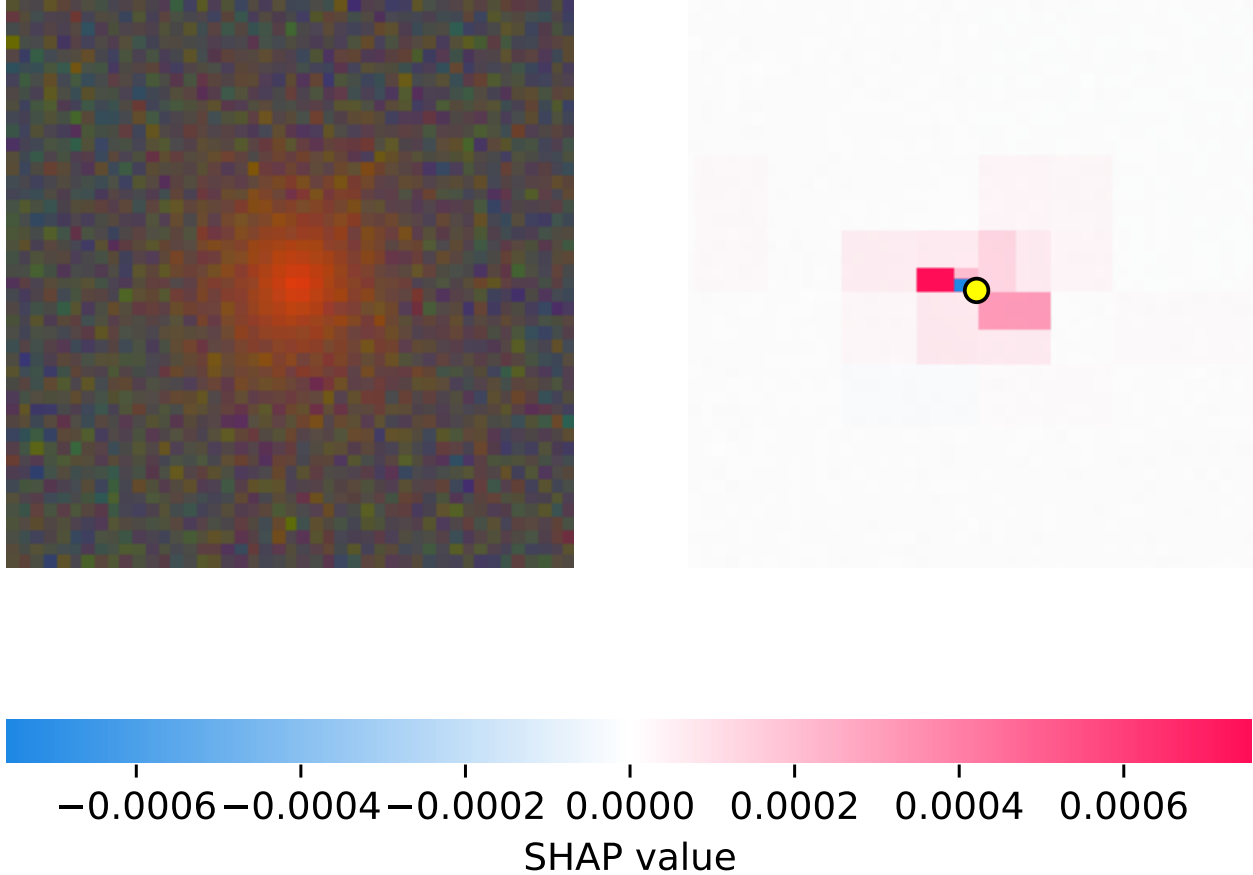


Figure 12: Example of a SHAP heatmap on the KiDS dataset (test). The yellow dot indicates the position of the most influential pixel according to SHAP. Each side corresponds to ≈ 9 arcsec.

Table 23: MAE of the models trained on the SDSS dataset. The results are taken on the test set and lens set for the models with the combination of hyperparameters with the best performance on the validation set. All numerical results are rounded to the third decimal place for consistency. The best results, and those falling within their confidence intervals, are highlighted in bold.

	SDSS
HOG + SVR	0.055 ± 0.000
A1	0.013 ± 0.000
A3	0.012 ± 0.000
NetZ	0.012 ± 0.000
PhotoZ	0.013 ± 0.000
EfficientNet	0.014 ± 0.000
MLPm	0.011 ± 0.000
ResNet	0.013 ± 0.000
SwinT	0.016 ± 0.000
Ensemble	0.013 ± 0.000
Improvement [%]	5

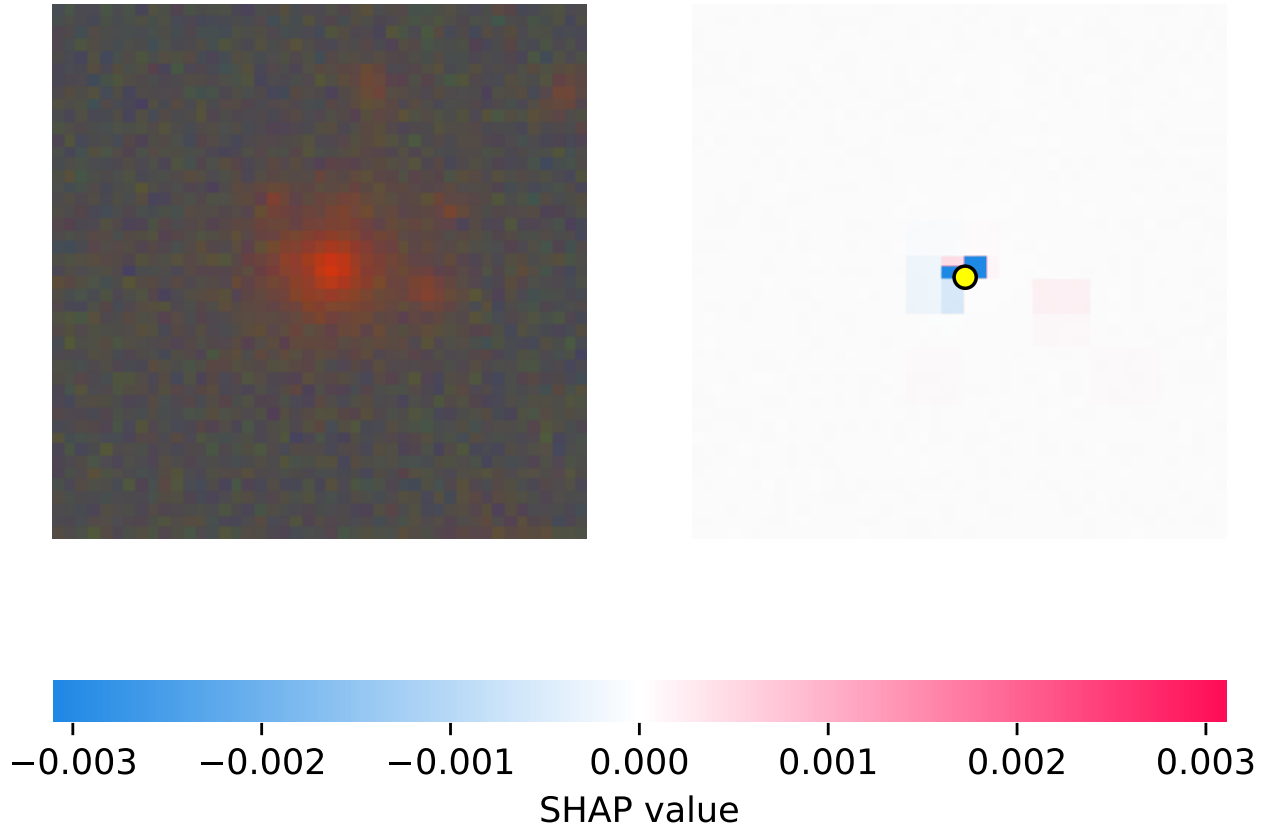


Figure 13: Example of a SHAP heatmap on the KiDS dataset (lens). The yellow dot indicates the position of the most influential pixel according to SHAP. Each side corresponds to ≈ 9 arcsec.

Table 24: NMAD of the models trained on the SDSS dataset. The results are taken on the test set and lens set for the models with the combination of hyperparameters with the best performance on the validation set. All numerical results are rounded to the third decimal place for consistency. The best results, and those falling within their confidence intervals, are highlighted in bold.

	SDSS
HOG + SVR	0.060 ± 0.001
A1	0.013 ± 0.000
A3	0.012 ± 0.000
NetZ	0.012 ± 0.000
PhotoZ	0.013 ± 0.000
EfficientNet	0.014 ± 0.000
MLPm	0.011 ± 0.000
ResNet	0.013 ± 0.000
SwinT	0.016 ± 0.000
Ensemble	0.013 ± 0.000
Improvement [%]	5

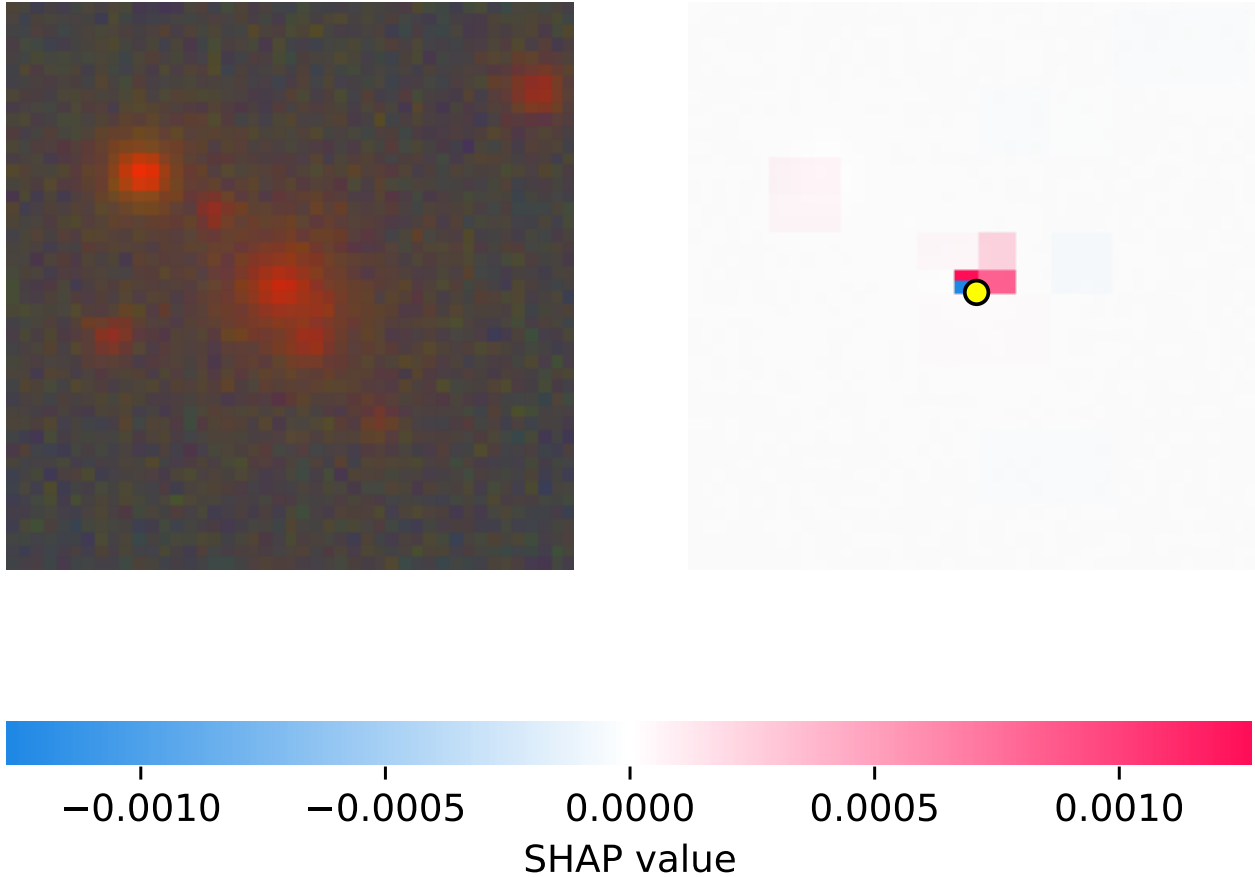


Figure 14: Example of a SHAP heatmap on the KiDS dataset (lens). The yellow dot indicates the position of the most influential pixel according to SHAP. Each side corresponds to ≈ 9 arcsec.

Table 25: σ_{68} of the models trained on the SDSS dataset. The results are taken on the test set and lens set for the models with the combination of hyperparameters with the best performance on the validation set. All numerical results are rounded to the third decimal place for consistency. The best results, and those falling within their confidence intervals, are highlighted in bold.

	SDSS
HOG + SVR	0.057 ± 0.000
A1	0.013 ± 0.000
A3	$\mathbf{0.012 \pm 0.000}$
NetZ	$\mathbf{0.012 \pm 0.000}$
PhotoZ	0.013 ± 0.000
EfficientNet	0.014 ± 0.000
MLPm	$\mathbf{0.012 \pm 0.000}$
ResNet	0.013 ± 0.000
SwinT	0.017 ± 0.000
Ensemble	0.013 ± 0.000
Improvement [%]	4

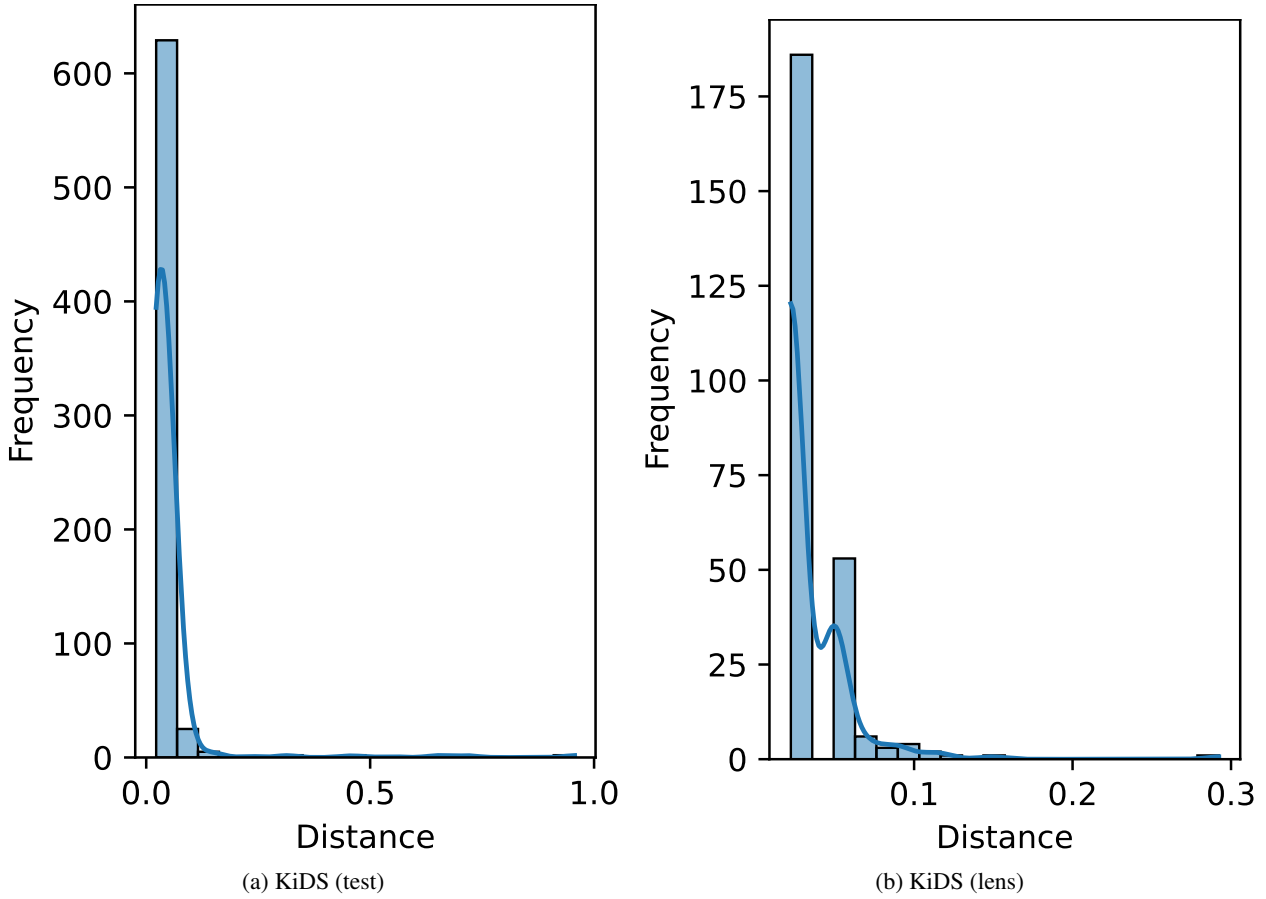


Figure 15: Distribution of the distances between the most influential pixels and the centres of the images for the KiDS dataset. The distances range between 0 and 1, where 1 indicates the maximum possible distance in a single image.

Table 26: Bias of the models trained on the SDSS dataset. The results are taken on the test set and lens set for the models with the combination of hyperparameters with the best performance on the validation set. All numerical results are rounded to the third decimal place for consistency. The best results, and those falling within their confidence intervals, are highlighted in bold.

	SDSS
HOG + SVR	0.024 ± 0.001
A1	0.001 ± 0.000
A3	$\mathbf{-0.000 \pm 0.000}$
NetZ	0.001 ± 0.000
PhotoZ	$\mathbf{0.000 \pm 0.000}$
EfficientNet	-0.003 ± 0.000
MLPm	$\mathbf{0.000 \pm 0.000}$
ResNet	0.003 ± 0.000
SwinT	0.001 ± 0.000
Ensemble	0.002 ± 0.000

Table 27: Outlier rate of the models trained on the SDSS dataset. The results are taken on the test set and lens set for the models with the combination of hyperparameters with the best performance on the validation set. All numerical results are rounded to the third decimal place for consistency. The best results, and those falling within their confidence intervals, are highlighted in bold.

SDSS	
HOG + SVR	0.412 ± 0.005
A1	0.008 ± 0.000
A3	0.006 ± 0.000
NetZ	0.008 ± 0.000
PhotoZ	0.012 ± 0.000
EfficientNet	0.012 ± 0.000
MLPm	0.006 ± 0.000
ResNet	0.010 ± 0.000
SwinT	0.018 ± 0.001
Ensemble	0.008 ± 0.000
Improvement [%]	0

above the best individual model. The marginal 5% improvement of MLPm in performance over the baseline models (HOG + SVR, A1 and A3) is relatively modest, indicating that the choice of the architecture is less relevant than in the other presented experiments. Overall, the best results are comparable to those of LSST-wide and DESI-DOT and demonstrate the effectiveness of the proposed deep architectures on datasets with different characteristics.

As observed in the other datasets, the better results of the DL algorithms presented in this work are also observed when comparing the R^2 scores. In this case, the DL architectures used in this work achieve $R^2 \approx 0.87$, compared to $R^2 \approx 0.33$ for baseline architectures. Still, the low average R^2 for the baseline architectures is influenced significantly by HOG + SVR ($R^2 \approx -0.81$). Considering the baseline DL architectures, the results are comparable ($R^2 \approx 0.90$) and similar to those of the best model ($R^2 \approx 0.91$).

On this dataset, using MAE as both the loss and early stopping criterion yields the best performance, reducing the test MAE by approximately 14% compared to the combination of MSE loss and R^2 for early stopping.

Table 24 and Table 25 present the results for the dispersion metrics NMAD and σ_{68} , respectively. Compared to the other datasets, the performance gap between the proposed architectures and the baselines is smaller. MLPm achieves the lowest NMAD (≈ 0.011), with a slight improvement of $\approx 5\%$ over the best baseline. For σ_{68} , the baseline architectures (e.g., A3 and NetZ) perform comparably to MLPm, with values of ≈ 0.012 . These results suggest that for the SDSS dataset, the increased complexity of the new architectures does not provide a significant advantage in scatter reduction over standard DL baselines. HOG + SVR remains significantly worse than all DL methods, with dispersion values more than 5 times higher than those of the best architecture. A paired bootstrap test (16th–84th percentile confidence interval) on NMAD confirms a statistically significant improvement of our best architecture over the baselines.

Table 26 shows that the majority of the DL architectures are unbiased. MLPm, PhotoZ, and A3 achieve a bias of 0.000, while others like EfficientNet show a small bias (≈ -0.003). HOG + SVR has a higher bias (≈ 0.024), further confirming its limitations compared to deep learning approaches.

Finally, Table 27 highlights the performance of DL models in rejecting outliers on this dataset. Most architectures, including the baselines (A1, A3, NetZ, PhotoZ) and the proposed MLPm, EfficientNet, and ensembling, achieve an outlier rate $< 1\%$, with A3 and MLPm being the best ones. Consequently, no significant improvement is observed, as both the baseline and advanced models effectively remove outliers. This result further indicates that the SDSS test set presents fewer challenges for these models compared to datasets like DES-deep or KiDS.

Training the optimal MLPm architecture on larger (90×90 pixel) images without resampling produced results comparable to NetZ and A3, albeit with higher errors than in the 45×45 pixel case.

Finally, the work in [72] reports competitive performance on SDSS using a deep capsule network and evaluates the results using σ_{MAD} , defined as:

$$\sigma_{MAD} = \text{median} \left(\left| \frac{\hat{y} - y}{1 + y} - \text{median} \left(\frac{\hat{y} - y}{1 + y} \right) \right| \right) \quad (10)$$

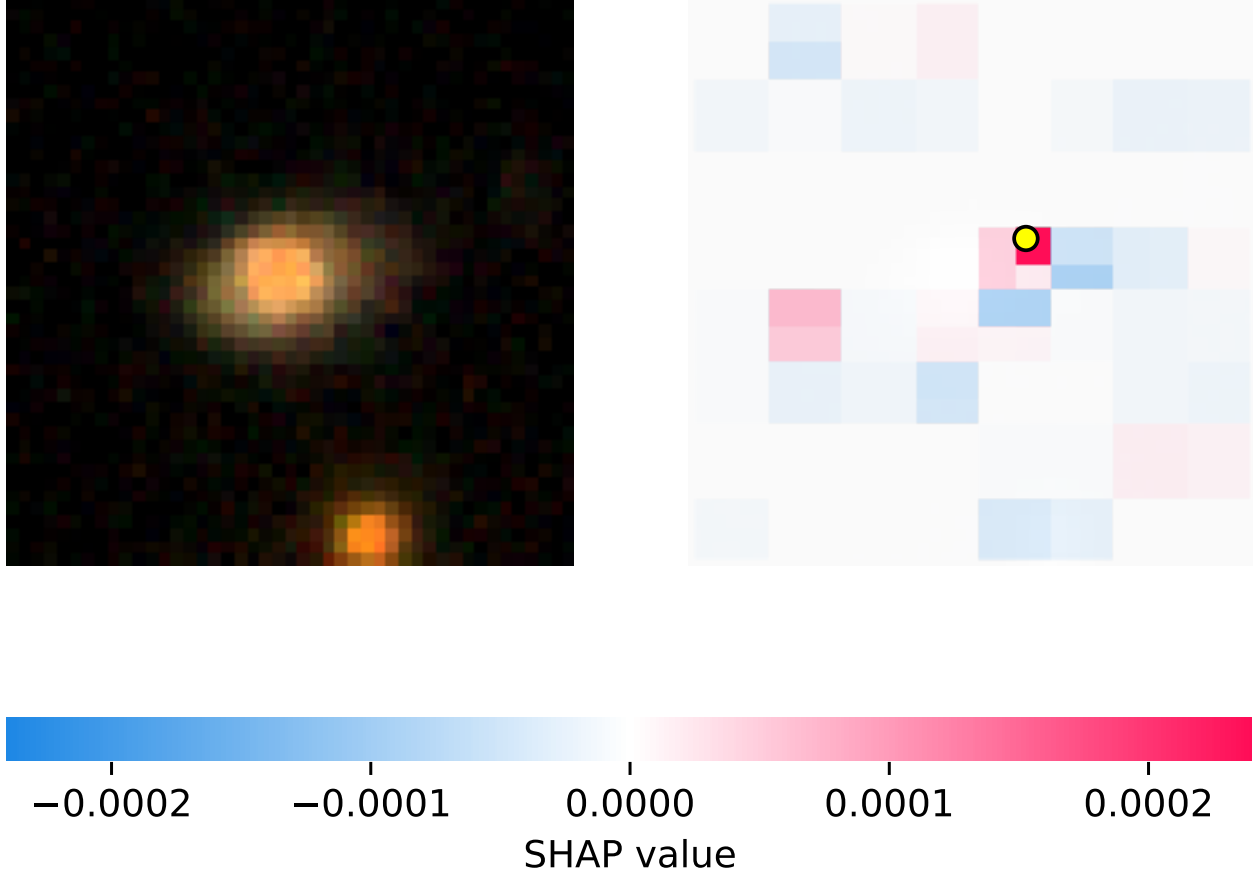


Figure 16: Example of a SHAP heatmap on the SDSS dataset. The yellow dot indicates the position of the most influential pixel according to SHAP. Each side corresponds to ≈ 18 arcsec.

They achieve $\sigma_{MAD} \approx 0.009$ using also auxiliary morphological class labels during training. In this work, we obtain better results ($\sigma_{MAD} \approx 0.008$) with MLPm and ResNet, which use only raw image data.

4.3.1 Explainability

Figures 16, 17, 18, and 19 show representative examples of SHAP heatmaps for SDSS galaxy redshift estimation obtained from the best-performing model. The model's focus changes based on the image content. Figure 16 shows the case of a diffuse heatmap caused by the presence of two sources, with the most influential pixel not aligned with the center of the central galaxy (the object of interest). Figure 17 and Figure 18, on the other hand, show that SHAP focuses only on the central parts of the images, as the sources are more compact, similar to the case of DESI-DOT. Finally, Figure 19 shows that the model focuses on the central part of the image, even if there are two bright bodies. In this case, the most influential pixel is correctly aligned with the center of the object of interest.

To quantify the relevance of the most influential pixels, Figure 20 shows the distribution of their distances from the image centre (normalised between 0 and 1), across the entire dataset. Overall, the mean distance is 0.065 and the median distance is 0.050, indicating the ability of the best model to focus on the galaxies for which redshift is estimated.

In this dataset, the average bounding box size is $\approx 58.94\%$ of the image, similar to KiDS, and the localization accuracy is 99.69%, comparable to the other datasets (except DES-deep).

4.4 Computational cost

This section analyzes the computational cost for training the proposed architectures on different datasets. Since the four DGL datasets have the same characteristics (image size and number of samples), they are analyzed together. All the architectures were trained on a single NVIDIA Ampere A100 GPU. Table 28 summarizes the training duration per epoch (in seconds), the total training time (in hours) for each architecture type across DGL, KiDS, and SDSS and the

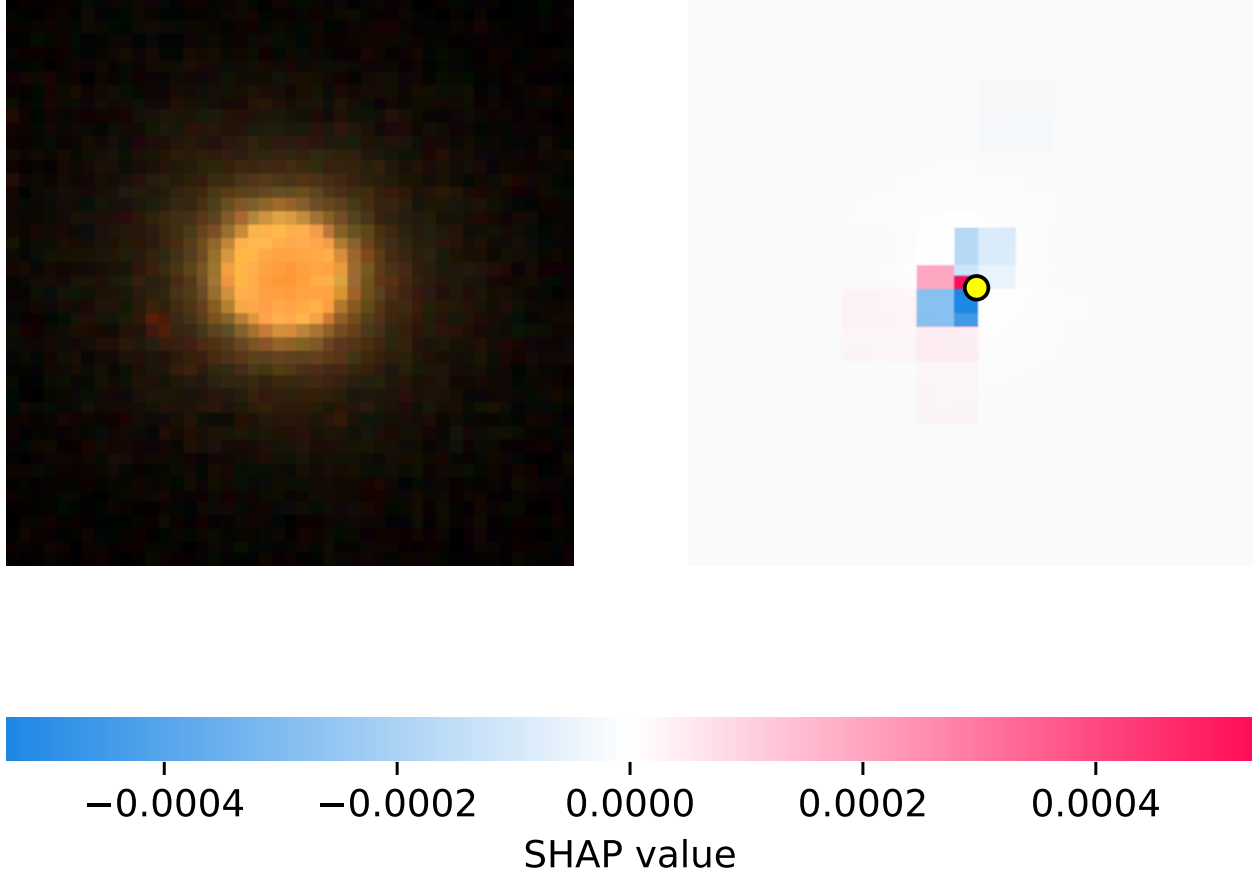


Figure 17: Example of a SHAP heatmap on the SDSS dataset. The yellow dot indicates the position of the most influential pixel according to SHAP. Each side corresponds to ≈ 18 arcsec.

cost of hyperparameter tuning. For each architecture, the reported training time refers to the hyperparameters leading to the highest parameters number and assumes no early stopping to provide a conservative estimate. The computational cost varies significantly depending on the architecture. ResNet is the most efficient architecture, requiring only 14 seconds per epoch on DGL and maintaining the lowest total training time across all scenarios (e.g., 10 hours for SDSS). EfficientNet is the most computationally expensive (e.g., 40 hours total for SDSS). The computational cost depends also by the dimension of the training set. Both DGL and KiDS are relatively small, allowing for rapid training (up to 4 hours per architecture). The SDSS dataset is characterized by a larger number of training samples and highlights the scaling challenge posed by large-scale astronomical surveys.

4.5 Threats to validity

Considering simulated gravitational lenses, real lens candidates, and non-lensed galaxies introduces threats to the validity of the proposed image-only pipeline. We identify three challenges regarding the interpretation and generalization of our results:

- Heterogeneous GT definitions: the definition of the target variable varies across datasets. While SDSS relies on spectroscopic redshifts, KiDS utilizes photometric estimates. Consequently, in the case of KiDS, the models approximate the output of a higher-dimensional estimator rather than predicting physical redshift directly.
- Morphological and PSF differences: the features correlating with redshift in Einstein rings can differ from those in standard spiral or elliptical galaxies. In addition, the difference between the idealized PSFs in simulations and the noise artifacts in real surveys challenges the models' ability to generalize. Still, this choice is unavoidable because of the limited number of confirmed gravitational lenses and gravitationally-lensed supernovae.

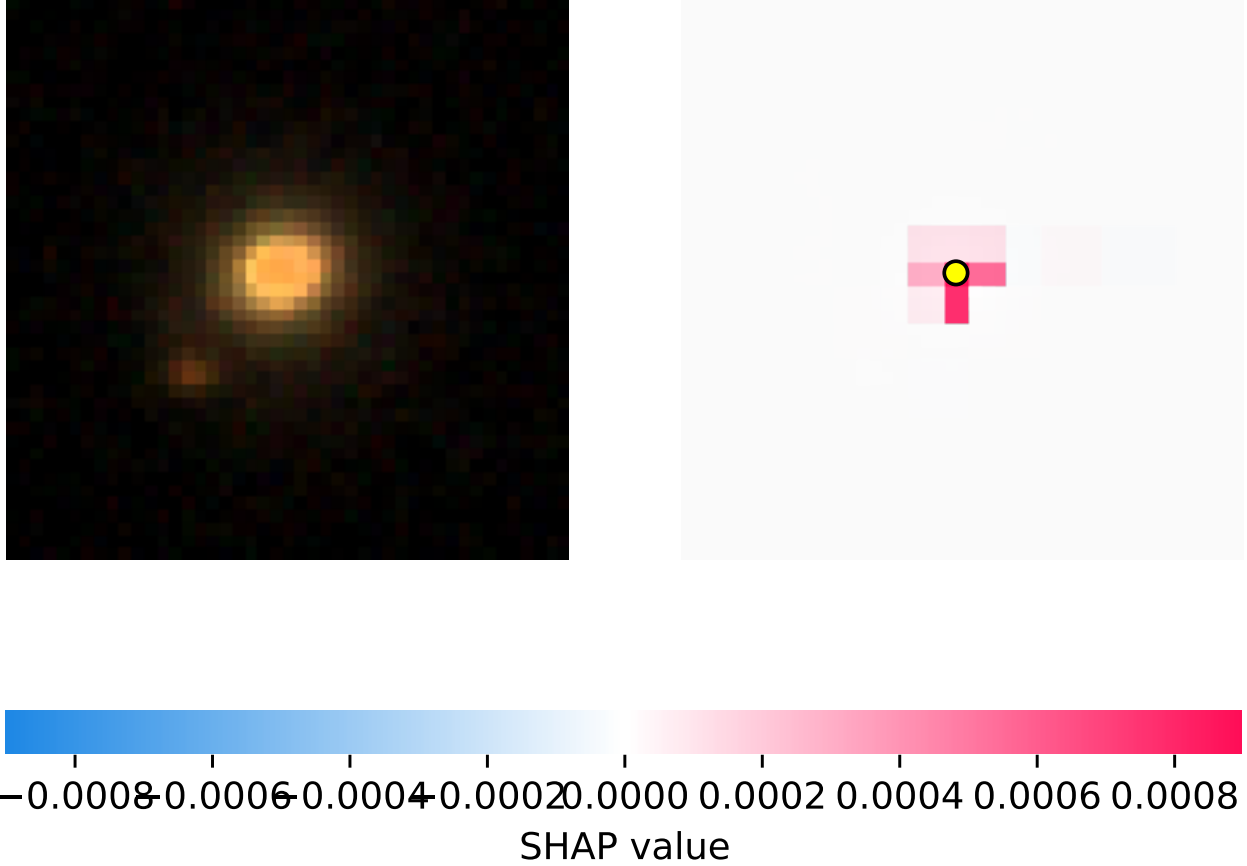


Figure 18: Example of a SHAP heatmap on the SDSS dataset. The yellow dot indicates the position of the most influential pixel according to SHAP. Each side corresponds to ≈ 18 arcsec.

- Unimodality limitations: by restricting the input to images, the pipeline neglects spectral features and additional multimodal information. The proposed approach relies on the ability of deep learning architectures to identify morphological and color-based features that correlate with redshift.

5 Conclusions and future work

This work focuses on redshift estimation using multi-channel simulated and real images of gravitationally-lensed supernovae, gravitational lenses, and galaxies. We propose DeepRed, a deep learning pipeline, based on computer vision models belonging to different families. More in detail, ResNet and EfficientNet are CNNs, MLPm relies on MLPs, and SwinT is attention-based. The results demonstrate the effectiveness of the models on datasets with different characteristics and the potential for accurately estimating redshift in both existing and upcoming real data. The results also highlight that all the architectures are less effective on noisy datasets. Overall, most of the deep learning models exhibit high R^2 scores (> 0.9) on most of the simulated datasets.

The results of HOG + SVR suggest that shape-based features capture only some information about redshift. Other existing architectures (A1, A3, PhotoZ and NetZ) have slightly better performance, but DeepRed DL architectures, based on convolutional and non-convolutional neural networks, and their ensembles, are better, on average, at redshift estimation.

On the DGL simulated datasets, EfficientNet is the best network on average, being particularly effective for DES-deep, a noisy dataset. In the other simulated datasets, most of the models exhibit similar behaviour ($R^2 > 0.9$). Ensembling the outputs of multiple networks further improves the results.

For the KiDS dataset, the best models are MLPm and SwinT. They learn to estimate redshift from low-probability lens candidates and are able to generalize to high-probability lens candidates.

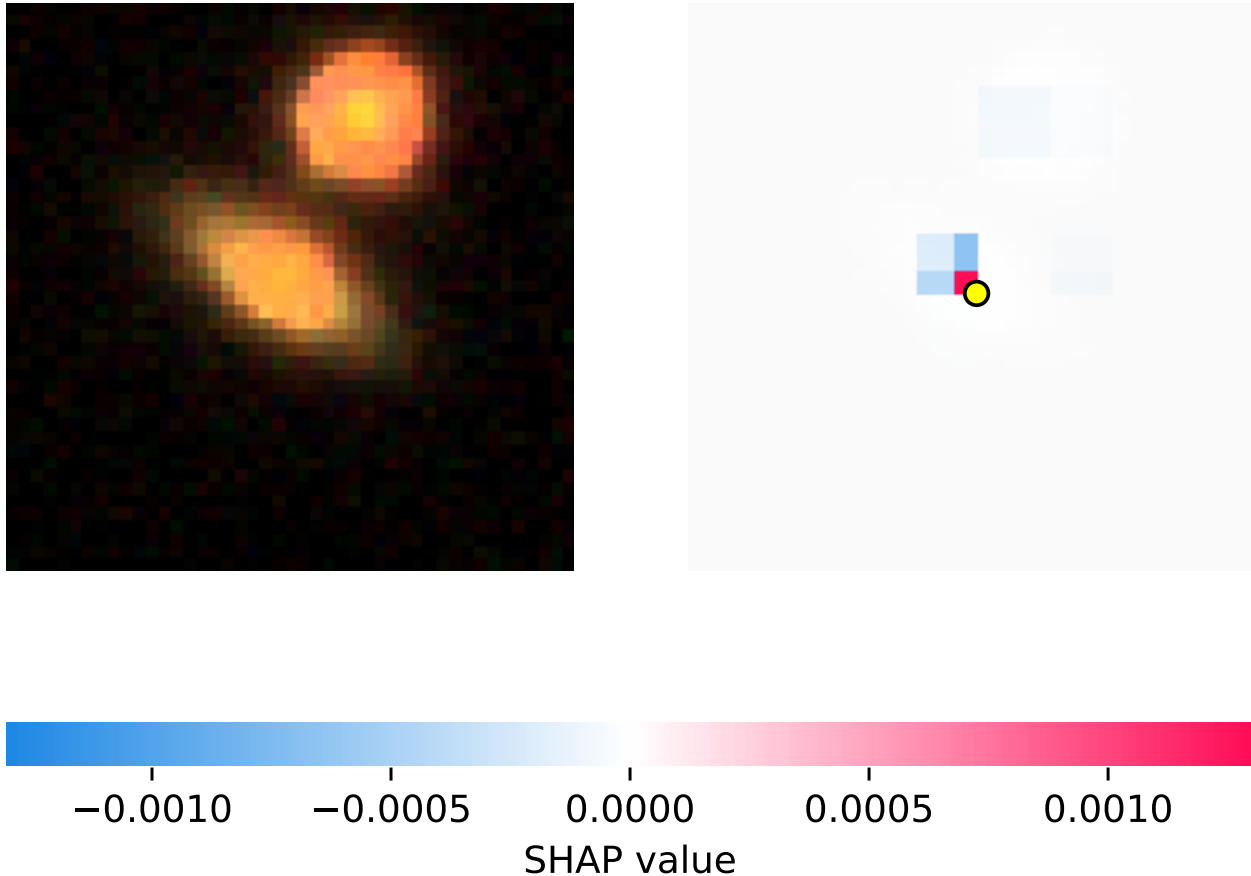


Figure 19: Example of a SHAP heatmap on the SDSS dataset. The yellow dot indicates the position of the most influential pixel according to SHAP. Each side corresponds to ≈ 18 arcsec.

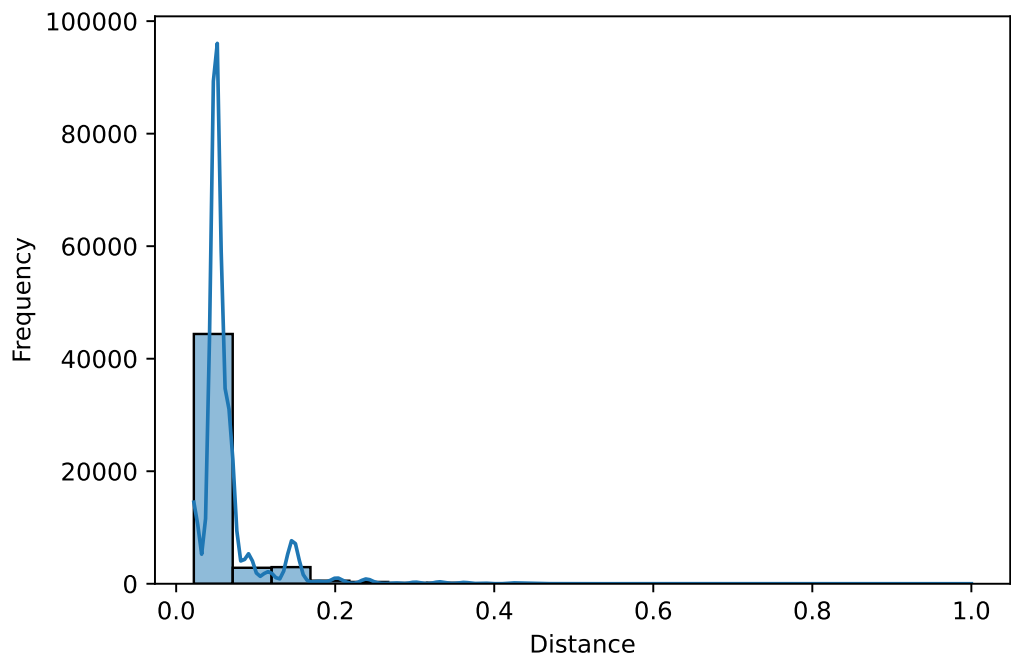


Figure 20: Distribution of the distances between the most influential pixels and the centres of the images for the SDSS dataset. The distances range between 0 and 1, where 1 indicates the maximum possible distance in a single image.

Table 28: Computational cost for training the proposed architectures on all the datasets

Model	Training time	DGL	KiDS	SDSS
SwinT	Epoch [s]	18	7	480
	Total [h]	3	1	13
	Hyperparameters tuning [h]	486	162	13
MLPm	Epoch [s]	24	8	840
	Total [h]	3	1	23
	Hyperparameters tuning [h]	324	108	23
ResNet	Epoch [s]	14	4	360
	Total [h]	2	1	10
	Hyperparameters tuning [h]	108	54	10
EfficientNet	Epoch [s]	26	12	1440
	Total [h]	4	2	40
	Hyperparameters tuning [h]	216	108	40
Ensemble	Total [h]	11	4	87
	Hyperparameters tuning [h]	1134	432	87

The SDSS dataset, different from DGL and KiDS, includes only non-lensed galaxies. Notably, the hyperparameters and models optimized on KiDS transfer effectively to SDSS, indicating good generalization. The architectures proposed in DeepRed prove robust for redshift estimation, outperforming the strongest baselines (A3 and NetZ) by $\approx 5\%$ in terms of MAE and NMAD.

The analysis of the models' explainability using SHAP shows that they give more importance to the central regions of the images on both the simulated and real datasets. This result is quantified using localization accuracy, higher than 95% on all the datasets except DES-deep. This dataset contains gravitational lenses that spread through the entire image and the images have a lower quality, which poses challenges also in terms of classification [26].

Future work can explore related research areas, including:

- Developing models that generalize across datasets and can be applied to data from different instruments.
- Incorporating time-series into the input data, similar to DGL [26], that classifies multimodal observations consisting of images and time series, and Hydra [36], that counts objects in the same multimodal data.
- Validating models on upcoming real observations, such as the ones from LSST, to identify new gravitationally-lensed supernovae, as proposed in [26], count objects in multimodal data [36], and estimate redshift.

To conclude, the proposed research directions serve as a foundation for applying interpretable DL algorithms to upcoming large sky surveys of astronomical data, aiming to estimate redshift accurately from images and multimodal data.

Acknowledgments

NOPV acknowledges support from INAF and CINECA for granting 125,000 core hours on the Leonardo supercomputer. We acknowledge Petrillo et al. (2019, MNRAS, 484, 3879), Li et al. (2020, ApJ, 899, L30) and Li et al. (2021, APJ, 923, 16). Based on observations made with ESO Telescopes at the La Silla Paranal Observatory under programme IDs 177.A-3016, 177.A-3017, 177.A-3018 and 179.A-2004, and on data products produced by the KiDS consortium. The KiDS production team acknowledges support from: Deutsche Forschungsgemeinschaft, ERC, NOVA and NWO-M grants; Target; the University of Padova, and the University Federico II (Naples). We acknowledge Kuijken et al. (2019, A&A 625, A2).

References

- [1] Bradley W. Carroll and Dale A. Ostlie. *An introduction to modern astrophysics*. Cambridge University Press.
- [2] Albert Einstein. Lens-like action of a star by the deviation of light in the gravitational field. 84(2188):506–507.
- [3] D. L. Jauncey, J. E. Reynolds, A. K. Tzioumis, T. W. B. Muxlow, R. A. Perley, D. W. Murphy, R. A. Preston, E. A. King, A. R. Patnaik, D. L. Jones, D. L. Meier, D. J. Bird, D. G. Blair, J. D. Bunton, R. W. Clay, M. E. Costa, R. A. Duncan, R. H. Ferris, R. G. Gough, P. A. Hamilton, D. W. Hoard, A. Kemball, M. J. Kesteven, E. T. Lobdell, A. N. Lurten, P. M. McCulloch, J. D. Murray, G. D. Nicolson, A. P. Rao, A. Savage, M. W. Sinclair, L. Skjerve, L. Taaffe, R. M. Wark, and G. L. White. An unusually strong einstein ring in the radio source PKS1830–211. 352(6331):132–134. Publisher: Nature Publishing Group.
- [4] Slava G. Turyshev and Viktor T. Toth. Wave-optical study of the einstein cross formed by a quadrupole gravitational lens. 104(12):124033. Publisher: American Physical Society.
- [5] Elisa Bernardini. Astronomy in the time domain. 331(6018):686–687. Publisher: American Association for the Advancement of Science.
- [6] A. Burrows and D. Vartanyan. Core-collapse supernova explosion theory. 589(7840):29–39. Publisher: Nature Publishing Group.
- [7] F. Ambrosino, A. Miraval Zanon, A. Papitto, F. Coti Zelati, S. Campana, P. D’Avanzo, L. Stella, T. Di Salvo, L. Burderi, P. Casella, A. Sanna, D. de Martino, M. Cadelano, A. Ghedina, F. Leone, F. Meddi, P. Cretaro, M. C. Baglio, E. Poretti, R. P. Mignani, D. F. Torres, G. L. Israel, M. Cecconi, D. M. Russell, M. D. Gonzalez Gomez, A. L. Riverol Rodriguez, H. Perez Ventura, M. Hernandez Diaz, J. J. San Juan, D. M. Bramich, and F. Lewis. Optical and ultraviolet pulsed emission from an accreting millisecond pulsar. 5(6):552–559. Publisher: Nature Publishing Group.
- [8] Gian Luca Israel, Roberta Amato, Matteo Imbrogno, Nicoló Oreste Pincioli Vago, and a Larger Team. Beyond accretion limits: The rise of pulsating gems. 346(1):e20240102. _eprint: <https://onlinelibrary.wiley.com/doi/pdf/10.1002/asna.20240102>.
- [9] F. Pintore, C. Pinto, G. Rodriguez-Castillo, G. L. Israel, N. O. Pincioli Vago, S. Motta, F. Barra, D. J. Walton, F. Fuerst, P. Kosec, C. Salvaggio, M. Del Santo, A. Wolter, M. Middleton, A. D’Aì, E. Ambrosi, L. Burderi, M. Imbrogno, R. Salvaterra, and A. Robba. A new pulsating neutron star in the ultraluminous x-ray source NGC 4559 x7? 695:A238. Publisher: EDP Sciences.
- [10] Nanda Rea. Fifty years of pulsar astrophysics. 1(12):829–830. Publisher: Nature Publishing Group.
- [11] Daniel J. Reardon, Robert Main, Stella Koch Ocker, Ryan M. Shannon, Matthew Bailes, Fernando Camilo, Marisa Geyer, Andrew Jameson, Michael Kramer, Aditya Parthasarathy, Renée Spiewak, Willem van Straten, and Vivek Venkatraman Krishnan. Bow shock and local bubble plasma unveiled by the scintillating millisecond pulsar j0437-4715. pages 1–11. Publisher: Nature Publishing Group.
- [12] Doogesh Kodi Ramanah, Nikki Arendse, and Radosław Wojtak. AI-driven spatio-temporal engine for finding gravitationally lensed type ia supernovae. 512(4):5404–5417.
- [13] Brandon Patel, Curtis McCully, Saurabh W. Jha, Steven A. Rodney, David O. Jones, Or Graur, Julian Merten, Adi Zitrin, Adam G. Riess, Thomas Matheson, Masao Sako, Thomas W.-S. Holoi, Marc Postman, Dan Coe, Matthias Bartelmann, Italo Balestra, Narciso Benítez, Rychard Bouwens, Larry Bradley, Tom Broadhurst, S. Bradley Cenko, Megan Donahue, Alexei V. Filippenko, Holland Ford, Peter Garnavich, Claudio Grillo, Leopoldo Infante, Stéphanie Jouvel, Daniel Kelson, Anton Koekemoer, Ofer Lahav, Doron Lemze, Dan Maoz, Elinor Medezinski, Peter Melchior, Massimo Meneghetti, Alberto Molino, John Moustakas, Leonidas A. Moustakas, Mario Nonino, Piero Rosati, Stella Seitz, Louis G. Strolger, Keiichi Umetsu, and Wei Zheng. THREE GRAVITATIONALLY LENSED SUPERNOVAE BEHIND CLASH GALAXY CLUSTERS. 786(1):9. Publisher: The American Astronomical Society.
- [14] Steven A. Rodney, Gabriel B. Brammer, Justin D. R. Pierel, Johan Richard, Sune Toft, Kyle F. O’Connor, Mohammad Akhshik, and Katherine E. Whitaker. A gravitationally lensed supernova with an observable two-decade time delay. 5(11):1118–1125. Publisher: Nature Publishing Group.
- [15] Dean Mamas. An explanation for the cosmological redshift. 23.
- [16] Maria Luiza Bedran. A comparison between the doppler and cosmological redshifts. 70(4):406–408.
- [17] Emory F. Bunn and David W. Hogg. The kinematic origin of the cosmological redshift. 77(8):688–694. Publisher: AIP Publishing.
- [18] Klaus Wilhelm and Bhola N. Dwivedi. On the gravitational redshift. 31:8–13.

- [19] David W. Hogg. Distance measures in cosmology.
- [20] Donald G. York, J. Adelman, John E. Anderson, Jr., Scott F. Anderson, James Annis, Neta A. Bahcall, J. A. Bakken, Robert Barkhouser, Steven Bastian, Eileen Berman, William N. Boroski, Steve Bracker, Charlie Briegel, John W. Briggs, J. Brinkmann, Robert Brunner, Scott Burles, Larry Carey, Michael A. Carr, Francisco J. Castander, Bing Chen, Patrick L. Colestock, A. J. Connolly, J. H. Crocker, István Csabai, Paul C. Czarapata, John Eric Davis, Mamoru Doi, Tom Dombeck, Daniel Eisenstein, Nancy Ellman, Brian R. Elms, Michael L. Evans, Xiaohui Fan, Glenn R. Federwitz, Larry Fiscelli, Scott Friedman, Joshua A. Frieman, Masataka Fukugita, Bruce Gillespie, James E. Gunn, Vijay K. Gurbani, Ernst de Haas, Merle Haldeman, Frederick H. Harris, J. Hayes, Timothy M. Heckman, G. S. Hennessy, Robert B. Hindsley, Scott Holm, Donald J. Holmgren, Chi-hao Huang, Charles Hull, Don Husby, Shin-ichi Ichikawa, Takashi Ichikawa, Zeljko Ivezic, Stephen Kent, Rita S. J. Kim, E. Kinney, Mark Klaene, A. N. Kleinman, S. Kleinman, G. R. Knapp, John Korieneck, Richard G. Kron, Peter Z. Kunszt, D. Q. Lamb, B. Lee, R. French Leger, Siriluk Limmongkol, Carl Lindenmeyer, Daniel C. Long, Craig Loomis, Jon Loveday, Rich Lucinio, Robert H. Lupton, Bryan MacKinnon, Edward J. Mannery, P. M. Mantsch, Bruce Margon, Peregrine McGehee, Timothy A. McKay, Avery Meiksin, Aronne Merelli, David G. Monet, Jeffrey A. Munn, Vijay K. Narayanan, Thomas Nash, Eric Neilsen, Rich Neswold, Heidi Jo Newberg, R. C. Nichol, Tom Nicinski, Mario Nonino, Norio Okada, Sadanori Okamura, Jeremiah P. Ostriker, Russell Owen, A. George Pauls, John Peoples, R. L. Peterson, Donald Pet travick, Jeffrey R. Pier, Adrian Pope, Ruth Pordes, Angela Prospicio, Ron Rechenmacher, Thomas R. Quinn, Gordon T. Richards, Michael W. Richmond, Claudio H. Rivetta, Constance M. Rockosi, Kurt Ruthmansdorfer, Dale Sandford, David J. Schlegel, Donald P. Schneider, Maki Sekiguchi, Gary Sergey, Kazuhiro Shimasaku, Walter A. Siegmund, Stephen Smee, J. Allyn Smith, S. Snedden, R. Stone, Chris Stoughton, Michael A. Strauss, Christopher Stubbs, Mark SubbaRao, Alexander S. Szalay, Istvan Szapudi, Gyula P. Szokoly, Anirudda R. Thakar, Christy Tremonti, Douglas L. Tucker, Alan Uomoto, Dan Vanden Berk, Michael S. Vogeley, Patrick Waddell, Shu-i Wang, Masaru Watanabe, David H. Weinberg, Brian Yanny, and Naoki Yasuda. The Sloan digital sky survey: Technical summary. 120(3):1579.
- [21] Adam G. Riess, Alexei V. Filippenko, Peter Challis, Alejandro Clocchiatti, Alan Diercks, Peter M. Garnavich, Ron L. Gilliland, Craig J. Hogan, Saurabh Jha, Robert P. Kirshner, B. Leibundgut, M. M. Phillips, David Reiss, Brian P. Schmidt, Robert A. Schommer, R. Chris Smith, J. Spyromilio, Christopher Stubbs, Nicholas B. Suntzeff, and John Tonry. Observational evidence from supernovae for an accelerating universe and a cosmological constant. 116(3):1009–1038.
- [22] Jan Kremer, Kristoffer Stensbo-Smidt, Fabian Gieseke, Kim Steenstrup Pedersen, and Christian Igel. Big universe, big data: Machine learning and image analysis for astronomy. 32(2):16–22.
- [23] Snigdha Sen, Sonali Agarwal, Pavan Chakraborty, and Krishna Pratap Singh. Astronomical big data processing using machine learning: A comprehensive review. 53(1):1–43.
- [24] Megan E. Schwamb, R. Lynne Jones, Peter Yoachim, Kathryn Volk, Rosemary C. Dorsey, Cyrielle Opitom, Sarah Greenstreet, Tim Lister, Colin Snodgrass, Bryce T. Bolin, Laura Inno, Michele T. Bannister, Siegfried Egg, Michael Solontoi, Michael S. P. Kelley, Mario Jurić, Hsing Wen LiN, Darin Ragozzine, Pedro H. Bernardinelli, Steven R. Chesley, Tansu Daylan, Josef Řurech, Wesley C. Fraser, Mikael Granvik, Matthew M. Knight, Carey M. Lisse, Renu Malhotra, William J. Oldroyd, Audrey Thirouin, and Quanzhi Ye. Tuning the legacy survey of space and time (LSST) observing strategy for solar system science. 266(2):22.
- [25] Mario Jurić, Jeffrey Kantor, K-T Lim, Robert H. Lupton, Gregory Dubois-Felsmann, Tim Jenness, Tim S. Axelrod, Jovan Aleksić, Roberta A. Allsman, Yusra AlSayyad, Jason Alt, Robert Armstrong, Jim Basney, Andrew C. Becker, Jacek Becla, Steven J. Bickerton, Rahul Biswas, James Bosch, Dominique Boutigny, Matias Carrasco Kind, David R. Ciardi, Andrew J. Connolly, Scott F. Daniel, Gregory E. Dauves, Frossie Economou, Hsin-Fang Chiang, Angelo Fausti, Merlin Fisher-Levine, D. Michael Freeman, Perry Gee, Philippe Gris, Fabio Hernandez, Joshua Hoblitt, Zeljko Ivezic, Fabrice Jammes, Darko Jevremović, R. Lynne Jones, J. Bryce Kalmbach, Vishal P. Kasliwal, K. Simon Krughoff, Dustin Lang, John Lurie, Nate B. Lust, Fergal Mullally, Lauren A. MacArthur, Peter Melchior, Joachim Moeyens, David L. Nidever, Russell Owen, John K. Parejko, J. Matt Peterson, Donald Pet travick, Stephen R. Pietrowicz, Paul A. Price, David J. Reiss, Richard A. Shaw, Jonathan Sick, Colin T. Slater, Michael A. Strauss, Ian S. Sullivan, John D. Swinbank, Schuyler Van Dyk, Veljko Vujčić, Alexander Withers, and Peter Yoachim. The LSST data management system.
- [26] Nicolò Oreste Pincioli Vago and Piero Fraternali. DeepGraviLens: a multi-modal architecture for classifying gravitational lensing data. 35(26):19253–19277.
- [27] P. O. Baqui, V. Marra, L. Casarini, R. Angulo, L. A. Díaz-García, C. Hernández-Monteagudo, P. A. A. Lopes, C. López-Sanjuan, D. Muniesa, V. M. Placco, M. Quartin, C. Queiroz, D. Sobral, E. Solano, E. Tempel, J. Varela, J. M. Vílchez, R. Abramo, J. Alcaniz, N. Benitez, S. Bonoli, S. Carneiro, A. J. Cenarro, D. Cristóbal-Hornillos, A. L. de Amorim, C. M. de Oliveira, R. Dupke, A. Ederoclite, R. M. González Delgado, A. Marín-Franch,

M. Moles, H. Vázquez Ramió, L. Sodré, and K. Taylor. The miniJPAS survey: star-galaxy classification using machine learning. 645:A87.

[28] P. C. H. Martens, G. D. R. Attrill, A. R. Davey, A. Engell, S. Farid, P. C. Grigis, J. Kasper, K. Korreck, S. H. Saar, A. Savcheva, Y. Su, P. Testa, M. Wills-Davey, P. N. Bernasconi, N.-E. Raouafi, V. A. Delouille, J. F. Hochdezel, J. W. Cirtain, C. E. DeForest, R. A. Angryk, I. De Moortel, T. Wiegemann, M. K. Georgoulis, R. T. J. McAteer, and R. P. Timmons. Computer vision for the solar dynamics observatory (SDO). 275(1):79–113.

[29] Hamed Valizadegan, Miguel J. S. Martinho, Laurent S. Wilkens, Jon M. Jenkins, Jeffrey C. Smith, Douglas A. Caldwell, Joseph D. Twicken, Pedro C. L. Gerum, Nikash Walia, Kaylie Hausknecht, Noa Y. Lubin, Stephen T. Bryson, and Nikunj C. Oza. ExoMiner: a highly accurate and explainable deep learning classifier that validates 301 new exoplanets. 926(2):120.

[30] Ben Henges, Jeyan Thiyagalingam, Connor Pettitt, Tony Hey, and Ofer Lahav. Deep learning methods for obtaining photometric redshift estimations from images. 512(2):1696–1709.

[31] S. Schuldt, S. H. Suyu, R. Cañameras, S. Taubenberger, T. Meinhardt, L. Leal-Taixé, and B. C. Hsieh. Photometric redshift estimation with a convolutional neural network: NetZ. 651:A55. Publisher: EDP Sciences.

[32] Changhua Li, Yanxia Zhang, Chenzhou Cui, Dongwei Fan, Yongheng Zhao, Xue-Bing Wu, Jing-Yi Zhang, Jun Han, Yunfei Xu, Yihan Tao, Shanshan Li, and Boliang He. Photometric redshift estimation of BASS DR3 quasars by machine learning. 509(2):2289–2303.

[33] Krishna Chunduri and Mithun Mahesh. Deep learning approach to photometric redshift estimation. In *2024 IEEE MIT undergraduate research technology conference (URTC)*, pages 1–5.

[34] Maggie Lieu. A comprehensive guide to interpretable AI-powered discoveries in astronomy. 11(6):187. Number: 6 Publisher: Multidisciplinary Digital Publishing Institute.

[35] Nicolò Oreste Pinciroli Vago and Piero Fraternali. DeepGraviLens.

[36] Nicolò Oreste Pinciroli Vago and Piero Fraternali. Multimodal multi-output ordinal regression for discovering gravitationally-lensed transients. 6(2):025067. Publisher: IOP Publishing.

[37] Brian Stalder, Kevin A. Reil, Chuck Claver, Ming Liang, Tei Wei Tsai, Travis Lange, Justine Haupt, Oliver Wiecha, Margaux Lopez, Gary Poczulp, Diane Hascall, Douglas R. Neill, Jacques Sebag, Brian Johnson, Neill Mills, Myung Cho, Homer A. Neal, Scott P. Newbry, Shawn Osier, Rafe Schindler, Dmitry Onoprienko, Anthony Johnson, R. Glenn Morris, Max Turri, Alan Eisner, Stephen A. Cisneros, Van Xiong, Michael E. Huffer, Gregg Thayer, Ronald Harris, Anthony Borstad, Anthony Tache, William Schoening, J. Anthony Tyson, Craig S. Lage, Merlin Fisher-Levine, Robert H. Lupton, Andres Plazas, Felipe Menanteau, Htut Khine Htay Win, Stephen Pietrowicz, and James Howard. Rubin commissioning camera: integration, functional testing, and lab performance. In Christopher J. Evans, Julia J. Bryant, and Kentaro Motohara, editors, *Ground-based and airborne instrumentation for astronomy VIII*, page 20. SPIE.

[38] B. Flaugher, H. T. Diehl, K. Honscheid, T. M. C. Abbott, O. Alvarez, R. Angstadt, J. T. Annis, M. Antonik, O. Ballester, L. Beaufore, G. M. Bernstein, R. A. Bernstein, B. Bigelow, M. Bonati, D. Boprie, D. Brooks, E. J. Buckley-Geer, J. Campa, L. Cardiel-Sas, F. J. Castander, J. Castilla, H. Cease, J. M. Cela-Ruiz, S. Chappa, E. Chi, C. Cooper, L. N. da Costa, E. Dede, G. Derylo, D. L. DePoy, J. de Vicente, P. Doel, A. Drlica-Wagner, J. Eiting, A. E. Elliott, J. Emes, J. Estrada, A. Fausti Neto, D. A. Finley, R. Flores, J. Frieman, D. Gerdes, M. D. Gladders, B. Gregory, G. R. Gutierrez, J. Hao, S. E. Holland, S. Holm, D. Huffman, C. Jackson, D. J. James, M. Jonas, A. Karcher, I. Karliner, S. Kent, R. Kessler, M. Kozlovsky, R. G. Kron, D. Kubik, K. Kuehn, S. Kuhlmann, K. Kuk, O. Lahav, A. Lathrop, J. Lee, M. E. Levi, P. Lewis, T. S. Li, I. Mandrichenko, J. L. Marshall, G. Martinez, K. W. Merritt, R. Miquel, F. Muñoz, E. H. Neilsen, R. C. Nichol, B. Nord, R. Ogando, J. Olsen, N. Palaio, K. Patton, J. Peoples, A. A. Plazas, J. Rauch, K. Reil, J.-P. Rheault, N. A. Roe, H. Rogers, A. Roodman, E. Sanchez, V. Scarpine, R. H. Schindler, R. Schmidt, R. Schmitt, M. Schubnell, K. Schultz, P. Schurter, L. Scott, S. Serrano, T. M. Shaw, R. C. Smith, M. Soares-Santos, A. Stefanik, W. Stuermer, E. Suchyta, A. Sypniewski, G. Tarle, J. Thaler, R. Tighe, C. Tran, D. Tucker, A. R. Walker, G. Wang, M. Watson, C. Weaverdyck, W. Wester, R. Woods, B. Yanny, and (The DES Collaboration). The dark energy camera. 150(5):150.

[39] M. Grespan, H. Thuruthipilly, A. Pollo, M. Lochner, M. Biesiada, and V. Etsebeth. TEGLIE: Transformer encoders as strong gravitational lens finders in KiDS: From simulations to surveys. 688:A34.

[40] Snigdha Sen, Ambuj Kumar Pandit, Pavan Chakraborty, and Krishna Pratap Singh. Performance evaluation of efficient interpretable CNN-transformer model for redshift prediction. 19(4):326.

[41] Johanna Pasquet, E. Bertin, M. Treyer, S. Arnouts, and D. Fouchez. Photometric redshifts from SDSS images using a convolutional neural network. 621:A26. Publisher: EDP Sciences.

- [42] Iqbal H. Sarker. Deep learning: a comprehensive overview on techniques, taxonomy, applications and research directions. 2(6).
- [43] Ashish Vaswani, Noam Shazeer, Niki Parmar, Jakob Uszkoreit, Llion Jones, Aidan N Gomez, Łukasz Kaiser, and Illia Polosukhin. Attention is all you need. In I. Guyon, U. Von Luxburg, S. Bengio, H. Wallach, R. Fergus, S. Vishwanathan, and R. Garnett, editors, *Advances in neural information processing systems*, volume 30. Curran Associates, Inc.
- [44] Alexey Dosovitskiy, Lucas Beyer, Alexander Kolesnikov, Dirk Weissenborn, Xiaohua Zhai, Thomas Unterthiner, Mostafa Dehghani, Matthias Minderer, Georg Heigold, Sylvain Gelly, Jakob Uszkoreit, and Neil Houlsby. An image is worth 16x16 words: Transformers for image recognition at scale. In *International conference on learning representations*.
- [45] Ze Liu, Yutong Lin, Yue Cao, Han Hu, Yixuan Wei, Zheng Zhang, Stephen Lin, and Baining Guo. Swin transformer: Hierarchical vision transformer using shifted windows. In *2021 IEEE/CVF International Conference on Computer Vision (ICCV)*, pages 9992–10002. ISSN: 2380-7504.
- [46] Billie F. Spencer, Vedhus Hoskere, and Yasutaka Narazaki. Advances in computer vision-based civil infrastructure inspection and monitoring. 5(2):199–222.
- [47] D.G. Lowe. Object recognition from local scale-invariant features. In *Proceedings of the seventh IEEE international conference on computer vision*, pages 1150–1157 vol.2. IEEE.
- [48] N. Dalal and B. Triggs. Histograms of oriented gradients for human detection. In *2005 IEEE computer society conference on computer vision and pattern recognition (CVPR'05)*, volume 1, pages 886–893 vol. 1.
- [49] John Canny. A computational approach to edge detection. PAMI-8(6):679–698.
- [50] Carmela Comito and Clara Pizzuti. Artificial intelligence for forecasting and diagnosing COVID-19 pandemic: A focused review. 128:102286.
- [51] Kaiming He, Xiangyu Zhang, Shaoqing Ren, and Jian Sun. Deep residual learning for image recognition. pages 770–778.
- [52] Shun Miao, Z. Jane Wang, and Rui Liao. A CNN regression approach for real-time 2d/3d registration. 35(5):1352–1363.
- [53] Pritisha Sarkar, Duranta Durbaar Vishal Saha, and Mousumi Saha. Real-time air quality index detection through regression-based convolutional neural network model on captured images. 34(1):e22276. _eprint: <https://onlinelibrary.wiley.com/doi/pdf/10.1002/tqem.22276>.
- [54] Jeroen P. A. Hoekendijk, Benjamin Kellenberger, Geert Aarts, Sophie Brasseur, Suzanne S. H. Poiesz, and Devis Tuia. Counting using deep learning regression gives value to ecological surveys. 11(1):23209. Publisher: Nature Publishing Group.
- [55] Ibomoiyi Domor Mienye and Yanxia Sun. A survey of ensemble learning: Concepts, algorithms, applications, and prospects. 10:99129–99149.
- [56] Y. Wang, Z. Pan, J. Zheng, L. Qian, and M. Li. A hybrid ensemble method for pulsar candidate classification. 364(8).
- [57] Saranya A. and Subhashini R. A systematic review of explainable artificial intelligence models and applications: Recent developments and future trends. 7:100230.
- [58] Ramprasaath R. Selvaraju, Michael Cogswell, Abhishek Das, Ramakrishna Vedantam, Devi Parikh, and Dhruv Batra. Grad-CAM: Visual explanations from deep networks via gradient-based localization. In *2017 IEEE international conference on computer vision (ICCV)*, pages 618–626. IEEE.
- [59] Federico Milani, Nicolò Oreste Pincioli Vago, and Piero Fraternali. Proposals generation for weakly supervised object detection in artwork images. 8(8):215. Number: 8 Publisher: Multidisciplinary Digital Publishing Institute.
- [60] Audrey Na. Improving convolutional neural networks diagnostic ability for malignant skin diseases on diverse skin tones with smooth grad-CAM++ and grad-CAM++. In *2024 International Conference on Electrical, Communication and Computer Engineering (ICECCE)*, pages 1–6.
- [61] Nicolò Oreste Pincioli Vago, Federico Milani, Piero Fraternali, and Ricardo da Silva Torres. Comparing CAM algorithms for the identification of salient image features in iconography artwork analysis. 7(7):106. Number: 7 Publisher: Multidisciplinary Digital Publishing Institute.
- [62] Marco Tulio Ribeiro, Sameer Singh, and Carlos Guestrin. “why should i trust you?”: Explaining the predictions of any classifier. In *Proceedings of the 22nd ACM SIGKDD international conference on knowledge discovery and data mining, Kdd '16*, pages 1135–1144. ACM.

[63] Alexander Binder, Grégoire Montavon, Sebastian Lapuschkin, Klaus-Robert Müller, and Wojciech Samek. Layer-wise relevance propagation for neural networks with local renormalization layers. In Alessandro E.P. Villa, Paolo Masulli, and Antonio Javier Pons Rivero, editors, *Artificial Neural Networks and Machine Learning – ICANN 2016*, pages 63–71. Springer International Publishing.

[64] Scott M Lundberg and Su-In Lee. A unified approach to interpreting model predictions. In I. Guyon, U. V. Luxburg, S. Bengio, H. Wallach, R. Fergus, S. Vishwanathan, and R. Garnett, editors, *Advances in neural information processing systems 30*, pages 4765–4774. Curran Associates, Inc.

[65] Ahmed M. Salih, Zahra Raisi-Estabragh, Ilaria Boscolo Galazzo, Petia Radeva, Steffen E. Petersen, Karim Lekadir, and Gloria Menegaz. A perspective on explainable artificial intelligence methods: SHAP and LIME. 7(1):2400304. Publisher: John Wiley & Sons, Ltd.

[66] A. HEWISH, S. J. BELL, J. D. H. PILKINGTON, P. F. SCOTT, and R. A. COLLINS. Observation of a rapidly pulsating radio source. 217(5130):709–713.

[67] Alberto Fernandez-Soto, Kenneth M. Lanzetta, Hsiao-Wen Chen, Sebastian M. Pascarelle, and Noriaki Yahata. On the compared accuracy and reliability of spectroscopic and photometric redshift measurements. 135(1):41–61.

[68] Gaël Noirot, Guillaume Desprez, Yoshihisa Asada, Marcin Sawicki, Vicente Estrada-Carpenter, Nicholas Martis, Ghassan Sarrouh, Victoria Strait, Roberto Abraham, Maruša Bradač, Gabriel Brammer, Kartheik Iyer, Shannon MacFarland, Jasleen Matharu, Lamiya Mowla, Adam Muzzin, Camilla Pacifici, Swara Ravindranath, Chris J Willott, Loïc Albert, René Doyon, John B Hutchings, and Neil Rowlands. The first large catalogue of spectroscopic redshifts in webb’s first deep field, SMACS j0723.3-7327. 525(2):1867–1884.

[69] Micol Bolzonella, Joan-Marc Miralles, and Roser Pello’. Photometric redshifts based on standard SED fitting procedures.

[70] I. Sadeh, F. B. Abdalla, and O. Lahav. ANNz2: Photometric redshift and probability distribution function estimation using machine learning. 128(968):104502.

[71] Nesar Ramachandra, Jonás Chaves-Montero, Alex Alarcon, Arindam Fadikar, Salman Habib, and Katrin Heitmann. Machine learning synthetic spectra for probabilistic redshift estimation: SYTH-z. 515(2):1927–1941.

[72] Biprateep Dey, Brett H Andrews, Jeffrey A Newman, Yao-Yuan Mao, Markus Michael Rau, and Rongpu Zhou. Photometric redshifts from SDSS images with an interpretable deep capsule network. 515(4):5285–5305.

[73] A. D’Isanto and K. L. Polsterer. Photometric redshift estimation via deep learning: Generalized and pre-classification-less, image based, fully probabilistic redshifts. 609:A111.

[74] R. Morgan, B. Nord, K. Bechtol, S. J. González, E. Buckley-Geer, A. Möller, J. W. Park, A. G. Kim, S. Birrer, M. Aguena, J. Annis, S. Bocquet, D. Brooks, A. Carnero Rosell, M. Carrasco Kind, J. Carretero, R. Cawthon, L. N. da Costa, T. M. Davis, J. De Vicente, P. Doel, I. Ferrero, D. Friedel, J. Frieman, J. García-Bellido, M. Gatti, E. Gaztanaga, G. Giannini, D. Gruen, R. A. Gruendl, G. Gutierrez, D. L. Hollowood, K. Honscheid, D. J. James, K. Kuehn, N. Kuropatkin, M. A. G. Maia, R. Miquel, A. Palmese, F. Paz-Chinchón, M. E. S. Pereira, A. Pieres, A. A. Plazas Malagón, K. Reil, A. Roodman, E. Sanchez, M. Smith, E. Suchyta, M. E. C. Swanson, G. Tarle, and C. To. DeepZipper: a novel deep-learning architecture for lensed supernovae identification. 927(1):109.

[75] Massimo Turatto. Classification of supernovae. In *Supernovae and gamma-ray bursters*, pages 21–36. Springer Berlin Heidelberg.

[76] Phil Marshall, Will Clarkson, Ohad Shemmer, Rahul Biswas, Miguel De Val-Borro, Jeonghee Rho, Lynne Jones, Timo Anguita, Stephen Ridgway, Federica Bianco, Ivezic, Zeljko, Michelle Lochner, Josh Meyers, Kathy Vivas, Melissa Graham, Chuck Claver, Seth Digel, Vishal Kasliwal, Peregrine M McGehee, Eric Gawiser, Eric Bellm, Lucianne Walkowicz, Knut Olsen, Peter Yoachim, Keaton Bell, David Nidever, Michael Lund, Andrew Connolly, Iair Arcavi, and Humna Awan. LSST science collaborations observing strategy white paper: “science-driven optimization of the LSST observing strategy”.

[77] T. M. C. Abbott, F. B. Abdalla, S. Allam, A. Amara, J. Annis, J. Asorey, S. Avila, O. Ballester, M. Banerji, W. Barkhouse, L. Baruah, M. Baumer, K. Bechtol, M. R. Becker, A. Benoit-Lévy, G. M. Bernstein, E. Bertin, J. Blazek, S. Bocquet, D. Brooks, D. Brout, E. Buckley-Geer, D. L. Burke, V. Busti, R. Campisano, L. Cardiel-Sas, A. Carnero Rosell, M. Carrasco Kind, J. Carretero, F. J. Castander, R. Cawthon, C. Chang, X. Chen, C. Conselice, G. Costa, M. Crocce, C. E. Cunha, C. B. D’Andrea, L. N. da Costa, R. Das, G. Dauves, T. M. Davis, C. Davis, J. De Vicente, D. L. DePoy, J. DeRose, S. Desai, H. T. Diehl, J. P. Dietrich, S. Dodelson, P. Doel, A. Drlica-Wagner, T. F. Eifler, A. E. Elliott, A. E. Evrard, A. Farahi, A. Fausti Neto, E. Fernandez, D. A. Finley, B. Flaugher, R. J. Foley, P. Fosalba, D. N. Friedel, J. Frieman, J. García-Bellido, E. Gaztanaga, D. W. Gerdes, T. Giannantonio, M. S. S. Gill, K. Glazebrook, D. A. Goldstein, M. Gower, D. Gruen, R. A. Gruendl, J. Gschwend, R. R. Gupta, G. Gutierrez, S. Hamilton, W. G. Hartley, S. R. Hinton, J. M. Hislop, D. Hollowood, K. Honscheid, B. Hoyle,

D. Huterer, B. Jain, D. J. James, T. Jeltema, M. W. G. Johnson, M. D. Johnson, T. Kacprzak, S. Kent, G. Khullar, M. Klein, A. Kovacs, A. M. G. Koziol, E. Krause, A. Kremin, R. Kron, K. Kuehn, S. Kuhlmann, N. Kuropatkin, O. Lahav, J. Lasker, T. S. Li, R. T. Li, A. R. Liddle, M. Lima, H. Lin, P. López-Reyes, N. MacCrann, M. A. G. Maia, J. D. Maloney, M. Manera, M. March, J. Marriner, J. L. Marshall, P. Martini, T. McClintock, T. McKay, R. G. McMahon, P. Melchior, F. Menanteau, C. J. Miller, R. Miquel, J. J. Mohr, E. Morganson, J. Mould, E. Neilsen, R. C. Nichol, F. Nogueira, B. Nord, P. Nugent, L. Nunes, R. L. C. Ogando, L. Old, A. B. Pace, A. Palmese, F. Paz-Chinchón, H. V. Peiris, W. J. Percival, D. Petracick, A. A. Plazas, J. Poh, C. Pond, A. Porredon, A. Pujol, A. Refregier, K. Reil, P. M. Ricker, R. P. Rollins, A. K. Romer, A. Roodman, P. Rooney, A. J. Ross, E. S. Rykoff, M. Sako, M. L. Sanchez, E. Sanchez, B. Santiago, A. Saro, V. Scarpine, D. Scolnic, S. Serrano, I. Sevilla-Noarbe, E. Sheldon, N. Shipp, M. L. Silveira, M. Smith, R. C. Smith, J. A. Smith, M. Soares-Santos, F. Sobreira, J. Song, A. Stebbins, E. Suchyta, M. Sullivan, M. E. C. Swanson, G. Tarle, J. Thaler, D. Thomas, R. C. Thomas, M. A. Troxel, D. L. Tucker, V. Vikram, A. K. Vivas, A. R. Walker, R. H. Wechsler, J. Weller, W. Wester, R. C. Wolf, H. Wu, B. Yanny, A. Zenteno, Y. Zhang, J. Zuntz, S. Juneau, M. Fitzpatrick, R. Nikutta, D. Nidever, K. Olsen, and A. Scott. The dark energy survey: Data release 1. 239(2):18.

[78] T. M. C. Abbott, S. Allam, P. Andersen, C. Angus, J. Asorey, A. Avelino, S. Avila, B. A. Bassett, K. Bechtol, G. M. Bernstein, E. Bertin, D. Brooks, D. Brout, P. Brown, D. L. Burke, J. Calcino, A. Carnero Rosell, D. Carollo, M. Carrasco Kind, J. Carretero, R. Casas, F. J. Castander, R. Cawthon, P. Challis, M. Childress, A. Clocchiatti, C. E. Cunha, C. B. D’Andrea, L. N. da Costa, C. Davis, T. M. Davis, J. De Vicente, D. L. DePoy, S. Desai, H. T. Diehl, P. Doel, A. Drlica-Wagner, T. F. Eifler, A. E. Evrard, E. Fernandez, A. V. Filippenko, D. A. Finley, B. Flaugher, R. J. Foley, P. Fosalba, J. Frieman, L. Galbany, J. García-Bellido, E. Gaztanaga, T. Giannantonio, K. Glazebrook, D. A. Goldstein, S. González-Gaitán, D. Gruen, R. A. Gruendl, J. Gschwend, R. R. Gupta, G. Gutierrez, W. G. Hartley, S. R. Hinton, D. L. Hollowood, K. Honscheid, J. K. Hoermann, B. Hoyle, D. J. James, T. Jeltema, M. W. G. Johnson, M. D. Johnson, E. Kasai, S. Kent, R. Kessler, A. G. Kim, R. P. Kirshner, E. Kovacs, E. Krause, R. Kron, K. Kuehn, S. Kuhlmann, N. Kuropatkin, O. Lahav, J. Lasker, G. F. Lewis, T. S. Li, C. Lidman, M. Lima, H. Lin, E. Macaulay, M. A. G. Maia, K. S. Mandel, M. March, J. Marriner, J. L. Marshall, P. Martini, F. Menanteau, C. J. Miller, R. Miquel, V. Miranda, J. J. Mohr, E. Morganson, D. Muthukrishna, A. Möller, E. Neilsen, R. C. Nichol, B. Nord, P. Nugent, R. L. C. Ogando, A. Palmese, Y.-C. Pan, A. A. Plazas, M. Pursiainen, A. K. Romer, A. Roodman, E. Rozo, E. S. Rykoff, M. Sako, E. Sanchez, V. Scarpine, R. Schindler, M. Schubnell, D. Scolnic, S. Serrano, I. Sevilla-Noarbe, R. Sharp, M. Smith, M. Soares-Santos, F. Sobreira, N. E. Sommer, H. Spinka, E. Suchyta, M. Sullivan, E. Swann, G. Tarle, D. Thomas, R. C. Thomas, M. A. Troxel, B. E. Tucker, S. A. Uddin, A. R. Walker, W. Wester, P. Wiseman, R. C. Wolf, B. Yanny, B. Zhang, and Y. Zhang. First cosmology results using type ia supernovae from the dark energy survey: Constraints on cosmological parameters. 872(2):L30.

[79] K. Kuijken, C. Heymans, A. Dvornik, H. Hildebrandt, J. T. A. de Jong, A. H. Wright, T. Erben, M. Bilicki, B. Giblin, H.-Y. Shan, F. Getman, A. Grado, H. Hoekstra, L. Miller, N. Napolitano, M. Paolilo, M. Radovich, P. Schneider, W. Sutherland, M. Tewes, C. Tortora, E. A. Valentijn, and G. A. Verdoes Kleijn. The fourth data release of the kilo-degree survey:ugriimaging and nine-band optical-IR photometry over 1000 square degrees. 625:A2.

[80] ESO Science Archive Facility. ESO science archive facility.

[81] I. K. Baldry, M. Alpaslan, A. E. Bauer, J. Bland-Hawthorn, S. Brough, M. E. Cluver, S. M. Croom, L. J. M. Davies, S. P. Driver, M. L. P. Gunawardhana, B. W. Holwerda, A. M. Hopkins, L. S. Kelvin, J. Liske, A. R. Lopez-Sánchez, J. Loveday, P. Norberg, J. Peacock, A. S. G. Robotham, and E. N. Taylor. Galaxy and mass assembly (GAMA): AUTOZ spectral redshift measurements, confidence and errors. 441(3):2440–2451.

[82] Sowmya Kochukrishnan, Premalatha Krishnamurthy, Yuvarajan D., and Nandagopal Kaliappan. Comprehensive study on the python-based regression machine learning models for prediction of uniaxial compressive strength using multiple parameters in charnockite rocks. 14(1):7360. Publisher: Nature Publishing Group.

[83] Mingxing Tan and Quoc V. Le. EfficientNet: Rethinking model scaling for convolutional neural networks.

[84] Ilya O Tolstikhin, Neil Houlsby, Alexander Kolesnikov, Lucas Beyer, Xiaohua Zhai, Thomas Unterthiner, Jessica Yung, Andreas Steiner, Daniel Keysers, Jakob Uszkoreit, Mario Lucic, and Alexey Dosovitskiy. MLP-mixer: An all-MLP architecture for vision. In M. Ranzato, A. Beygelzimer, Y. Dauphin, P.S. Liang, and J. Wortman Vaughan, editors, *Advances in neural information processing systems*, volume 34, pages 24261–24272. Curran Associates, Inc.

[85] Stéphane Lathuilière, Pablo Mesejo, Xavier Alameda-Pineda, and Radu Horaud. A comprehensive analysis of deep regression. 42(9):2065–2081.

[86] Ian T. Jolliffe and Jorge Cadima. Principal component analysis: a review and recent developments. 374(2065):20150202.

- [87] Muhammad Shafiq and Zhaoquan Gu. Deep residual learning for image recognition: a survey. 12(18):8972.
- [88] Baoru Han, Han Wang, Dawei Qiao, Jia Xu, and Tianyu Yan. Application of zero-watermarking scheme based on swin transformer for securing the metaverse healthcare data. 28(11):6360–6369.
- [89] Leo Breiman. Stacked regressions. 24(1):49–64.
- [90] Pierre Dardouillet, Alexandre Benoit, Emna Amri, Philippe Bolon, Dominique Dubucq, and Anthony Credoz. Explainability of image semantic segmentation through SHAP values. In *Pattern recognition, computer vision, and image processing. ICPR 2022 international workshops and challenges*, pages 188–202. Springer Nature Switzerland.
- [91] Angus H. Wright, Hendrik Hildebrandt, Jan Luca van den Busch, Maciej Bilicki, Catherine Heymans, Benjamin Joachimi, Constance Mahony, Robert Reischke, Benjamin Stölzner, Anna Wittje, Marika Asgari, Nora Elisa Chisari, Andrej Dvornik, Christos Georgiou, Benjamin Giblin, Henk Hoekstra, Priyanka Jalan, Anjitha John William, Shahab Joudaki, Konrad Kuijken, Giorgio Francesco Lesci, Shun-Sheng Li, Laila Linke, Arthur Loureiro, Matteo Maturi, Lauro Moscardin, Lucas Porth, Mario Radovich, Tilman Tröster, Maximilian von Wietersheim-Kramsta, Ziang Yan, Mijin Yoon, and Yun-Hao Zhang. KiDS-legacy: Redshift distributions and their calibration. 703:A144.